Biophysical mechanisms that maintain biodiversity through trade-offs

MS / tracking No. NCOMMS-14-09495A

Justin R. Meyer[1], Ivana Gudelj[2] & Robert Beardmore[2]

[1] Division of Biology, University of California, San Diego, La Jolla, CA 92093, US
[2] Biosciences, Geoffrey Pope, University of Exeter, Stocker Road, Exeter EX4 4QD, UK

r.e.beardmore@exeter.ac.uk ; jrmeyer@ucsd.edu

Trade-offs are thought to arise from inevitable, biophysical limitations that prevent organisms from optimising multiple traits simultaneously. A leading explanation for biodiversity maintenance is a theory that if the shape, or geometry, of a trade-off is right, then multiple species can coexist. Testing this theory, however, is difficult as trait data is usually too noisy to discern shape, or trade-offs necessary for the theory are not observed *in vivo*. To address this, we infer geometry directly from the biophysical mechanisms that cause trade-offs, deriving the geometry of two by studying nutrient uptake and metabolic properties common to all living cells. To test for their presence *in vivo* we isolated *Escherichia coli* mutants that vary in a nutrient transporter, LamB, and found evidence for both trade-offs. Consistent with data, population genetics models incorporating the trade-offs successfully predict the co-maintenance of three distinct genetic lineages, demonstrating that trade-off geometry can be deduced from fundamental principles of living cells and used to predict stable genetic polymorphisms.

Introduction

Trade-offs between life history traits are seen as a key part of the processes that maintain the rich biodiversity observed in microbes,[1] plants,[2] insects[3] and rain forests.[4] Due to its importance to biodiversity theory, a search for trade-off data has become the subject of a burgeoning experimental literature using microbial populations in the laboratory.[1,5–12] However, despite the significance of trade-off geometry to the theory and the

long-postulated hypothesis that trade-offs arise from life-history constraints, we know of no successful derivation of trade-off geometry in living systems from fundamental physical or biochemical principles. Resolving this absence is critical if we are to successfuly predict conditions that maintain diverse microbial communities. Here we present a mechanistic theory, supported by data, on the geometry of two trade-offs among microbes: one is a feeding trade-off, one is a growth trade-off. These trade-offs have been studied before but their shapes have remained elusive, yet here we find agreement between theory and data showing that one trade-off is convex and the other is sigmoidal and both are implicated in diversity maintenance.

The first trade-off we study is the metabolic rate-yield trade-off (the RYTO or 'waste from haste' trade-off[13,14]) whose shape we found by culturing *Escherichia coli* at different growth rates. The second trade-off shape we deduce is that of the nutrient uptake rate-affinity trade-off (the RATO[14,15]) by measuring the growth kinetics of a library of mutant *E. coli* that varied in a sugar transporter, LamB. Given these two geometries, prior theory predicts that there could be nutrient conditions where divergent consumer strategies would coexist in a microbial population.[16] To test this, we used bespoke theoretical population genetics models to determine environmental conditions that would support a multiplicity of nutrient transporter genotypes in *E. coli*. However, this theory successfully predicted the frequency dynamics of three genetic lineages in a laboratory microcosm only when it incorporated two trade-offs, not one. We therefore establish that trade-offs are a consequence of the physical necessities of life and moreover, genetic polymorphisms and biodiversity patterns can be predicted from the resulting trade-off geometries.

Results

Many mechanisms have been proposed for the RYTO in bacteria, both physiological[17] and metabolic,[13] and a quadratic shape is thought to describe it.[13] Attempts to find the RYTO *in vivo*, however, have been mixed. A negative correlation between growth rate and yield has been observed but without the quadratic form.[12] Moreover, positive rate-yield correlations, the antithesis of a rate-yield trade-off, have been observed in other bacterial species[9] and, curiously, this relationship is also predicted to be constrained by

a quadratic geometry.[10] We can reconcile these apparent contradictions by following a suggestion[9] that r-k relationships can be manipulated by varying the carbon richness of the environment in which bacteria grow (for clarity, we use k for carrying capacity where others use K). We hypothesize that r and k are indeed positively correlated and that the shape of the RYTO can be extracted from r-k datasets.

To study the RYTO, we cultured *E.coli B* (REL606) in Davis minimal (DM) medium supplemented with a range of sugar (maltotriose) concentrations. We determined their r (exponential growth rate) and k (maximal population size) values by fitting the mathematical logistic model $\frac{d}{dt}x = rx(1 - x/k)$ to growth data, where $x(t)$ denotes bacterial population density at time t (Supplementary Discussion, section C). At low sugar concentrations, ranging from 1 to $8\mu g/ml$ the experiment recapitulates a prior dataset[9] whereby a positive, linear correlation between r and k is observed (Figure 1a). However, when observations from higher maltotriose concentrations are added to the data, ranging from 1 to $125\mu g/ml$, the r-k relationship becomes nonlinear because r saturates. This is expected because growth rate is limited whereas k increases proportionally to the maltotriose supplied (Figure 1a, Supplementary Fig. 15). Although r and k adaptation are classically viewed as conflicting life history strategies[18] here they are positively correlated. Nevertheless, this is still consistent with a RYTO, as we now explain.

Assume, for the moment, that c is a constant representing the biomass yield of *E.coli* per maltotriose, when cultured with maltotriose as the sole carbon source at supply concentration $S_0\mu g/ml$. We assume Monod growth kinetics, so the bacterial population density B changes as $\frac{d}{dt}B = cBV_{\max}S/(K_m + S)$ and maltotriose reduces in concentration as $\frac{d}{dt}S = -BV_{\max}S/(K_m + S)$, where $V_{\max}$ is the maximal rate of uptake of maltotriose and K_m is the maltotriose half saturation constant. The initial condition $S(0) = S_0$ applies here, $B(0)$ represents a bacterial inoculate whose size is assumed negligibly small.

A conservation law holds in this model, $B(t)/c + S(t) = B(0)/c + S_0$, so that when $S \approx 0$ at carrying capacity, $k = B \approx c \cdot S_0$ thus k is proportional to the maltoriose supplied, if we neglect $B(0)$. If we approximate exponential growth using the Monod model, so $r \approx cV_{\max}S_0/(K_m + S_0)$, then $k/r \approx (K_m + S_0)/V_{\max}$ and so k and k/r should both exhibit linear dependence on S_0, hence k and r should be positively correlated. This is

consistent with our observations (for k versus S_0: $R^2 > 0.99, p < 10^{-8}$; for k/r versus S_0: $R^2 \approx 0.93, p < 10^{-4}$; Supplementary Fig. 15). However, observations also indicate that yield, meaning c or k/S_0, is not constant because it decreases with increasing maltotriose supply (Figure 1b, F-test versus constant model, $F = 17.3, p < 0.00014$).

We therefore need a more accurate description of the variable yield data in Figure 1c. So, we relax our assumption that yield is a constant independent of the carbon supplied. Maltotriose import and metabolism is carried out by the genes of the *mal* regulon.[19] This set is induced by *malT*, which itself is expressed when maltodextrins like maltotriose are present. The uptake of maltodextrins is facilitated by the LamB maltoporin in combination with the periplasmic maltodextrin-binding protein MalE and the ATP-driven inner-membrane transport system $\mathrm{MalGFK_2}$. Once in the cytoplasm maltotriose is degraded by MalZ into maltose and glucose, MalQ then produces two glucoses for each available maltose. Given this, a theoretical form for the rate and yield of maltose metabolism can be derived (Supplementary Discussion, section B) by representing glycolysis and the TCA cycle as a branched pathway[20] (Figure 1a). Using ATP yield as a proxy for biomass yield, this model predicts a relationship between carbon supply, S_0, and cell yield. Writing $c(S_0)$ to represent this relationship, it has the following repression-activation form

$$c(S_0) = c_{\mathrm{hi}} \frac{1}{1 + pS_0} + \frac{pS_0}{1 + pS_0} c_{\mathrm{lo}}. \tag{1}$$

Here c_{hi} represents the highest yield attainable, achieved at the lowest sugar concentrations, whereas c_{lo} is the yield attained when sugar is abundant, p is a phenotype that controls the rate of decrease in yield with increasing sugar supply.

The positive r-k correlation predicted by the constant and variable-yield assumptions are consistent with r-k data (Figure 1b) with agreement across two orders of magnitude of maltotriose supply in both cases. However, only the decreasing yield model correctly captures the yield data across the full range of maltotriose concentrations (Figure 1c, $R^2 > 0.99, p \ll 10^{-15}$ from above F-test). The resulting 5-parameter, within-strain geometric RYTO model

$$(\text{growth rate}, \text{cell yield}) = \left(c(S_0) \frac{S_0 V_{\max}}{K_m + S_0}, c(S_0) \right) \tag{2}$$

has a sigmoidal shape that compares favourably with data (Figure 1c). Note that (2) only has only 4 independent parameters, $V_{\max}$ merely converts cell yield into a rate.

The logistic equation contains no explicit term for nutrient availability so, we deployed the following improvement to that model that better captures different bacterial growth phases and which can also represent N-strain, frequency- and density-dependent competition for maltotriose (where $N \geq 1$):

$$\frac{d}{dt}B_i = \nu n_i + G_i(S)B_i,\ \frac{d}{dt}S = -\sum_{i=1}^{N} U_i(S)B_i,\ \frac{d}{dt}n_i = -\nu n_i. \tag{3}$$

Here B_i is density of the i-th strain, growth rate is $G_i(S) := c_i \cdot U_i(S)$, c_i is cell yield and $U_i(S)$ is nutrient uptake rate (at nutrient concentration S):

$$U_i(S) := \frac{V^i_{\max} S}{K^i_m + S}. \tag{4}$$

The variable n_i represents a subpopulation of the inoculate that may be in a non-vegetative state and the associated ν_i-dependent terms allow the model to capture the transition from lag to exponential phase. When $N = 1$ equation (3) is consistent with the RYTO data for *E.coli* strain REL606 (Supplementary Fig. 14) and when $N > 1$, it can predict the outcome of multi-strain competition experiments (Supplementary Discussion, section C).

Pursuing evidence of a between-strain RYTO, we generated a library of *E. coli* mutants that vary in growth rate because of mutations that interfere with maltotriose uptake. *E. coli* uses LamB to transport maltotriose across the outer membrane however it may also be taken up by OmpF, albeit over an order of magnitude more slowly[21,22]. LamB is also a receptor for the virus λ, which provides a convent way to generate LamB mutations. Previous work has shown that when *E. coli* and λ are co-cultured, *E. coli* rapidly evolves resistance through an array of *lamB* mutations [23,24], some of which alter the diffusion of maltodextrins across the outer membrane by altering the pore dimensions[25]. We therefore co-cultured 100 separate populations in batch for three days and isolated two bacteria per population. The large number of populations and low sampling intensity within each population helped maximize the number of unique *lamB* mutants isolated, the short time period ensured only a single mutation occurred in the *lamB* gene and nowhere else in the genome. Altogether we harvested 50 novel *E.coli* strains with SNPs, insertions and deletions in the *lamB* gene, the library also includes frameshift mutations that render LamB inoperable (Supplementary Table 1).

We estimated uptake rate, yield and therefore growth rate for each strain by culturing them separately in DM media supplemented with 10, 25 and 250$\mu g/ml$ maltotriose by

fitting (3) to that data (Supplementary Discussion, section C). This consistently produced similar values for yield between strains and environments and ignificant evidence for a negative rate-yield correlation between strains was observed but only at a maltotriose concentration of $250\mu g/ml$, not at $25\mu g/ml$ ($p < 0.00064$ and $p > 0.16$ respectively; see Figure 2a).

The same dataset points to a second possible trade-off: a correlation between K_m and $V_{\max}$ (Figure 3a, $R^2 \approx 0.58, F \approx 70.5, p < 10^{-10}$). This prediction is consistent with prior single transporter models for small-molecule uptake which show that changes to a transporter's affinity for the molecule will produce concomitant changes in its maximal translocation rate.[26–28] This was demonstrated by distorting the performance of transmembrane channels by creating potential energy wells within a synthetic pore using holographic tweezers. These experiments showed that an optimal transporter configuration must balance a high translocation probability and 'not too long' a blockage of the channel;[27] this is the physical basis of the RATO.

Different theories are possible for RATO geometries depending on the assumptions they use. A linear relationship between K_m and $V_{\max}$ can be derived[27] (in particular, their equation (6)) whereby $K_m = pV_{\max} + q$ for parameters (p, q). This result is consistent with a theoretical enzymatic model based on a transporter embedded within a single membrane (Supplementary Discussion, section B), so this would appear to be the description of the trade-off we seek. However, affinity for a carbon source, a, is usually defined by $a := \frac{dU}{dS}(0) = V_{\max}/K_m$ and so strains with different $V_{\max}$ and K_m phenotypes could have a common maltotriose affinity, if $q = 0$. However, RATO data observed between the *E. coli* library strains is too noisy to eliminate linearity or to resolve shape (Figure 3a). To remedy this, we used a related *Saccharomyces cerevisiae* dataset where glucose transporters had been genetically manipulated.[26] As this data exhibits significant nonlinearity (see Figure 3b for the relative likelihoods, $\mathsf{RL}_{\mathsf{linear}}$, of linear and nonlinear datafits where $\mathsf{RL}_{\mathsf{linear}} < 0.013$), the prior argument supporting a linear K_m-$V_{\max}$ relationship will thus have to be modified.

On reflection, small molecule uptake in some microbes is a two-step process: entry into the cytoplasm of Gram-negative bacteria and yeast requires the passage through two diffusive

barriers, not one. Modifying the above single membrane model to account for this, K_m depends nonlinearly on $V_{\max}$ in the resulting theory (Supplementary Discussion, section B):

$$K_m \approx \frac{pV_{\max}^2 + qV_{\max} + r}{1 + sV_{\max}}, \tag{5}$$

where (p, q, r, s) are parameters. A quadratic nonlinearity here is expected because if transport through one diffusive barrier leads to a linear K_m-$V_{\max}$ relationship, two barriers positioned in serial separated by a periplasm should produce a quadratic-like function, which (5) is. A power-law fit to empirical $(V_{\max}, K_m)$ data of the form $K_m \approx a \cdot V_{\max}^b$ is consistent with (5) because $b \approx 1.86 \pm 0.23$ (mean $\pm$ estimated s.e.m., $df = 8$, Figure 3b). We note that the role played by MalE in *E.coli* is neglected as part of the derivation of (5) (in Supplementary Discussion, section B), but if we were to assume that MalE-maltotriose binding is so rapid that no free maltotriose is found in the periplasm, then the form of (5) will not change.

To test whether the RATO could promote the maintenance of bacterial diversity, we isolated a subset of our library that exhibited a RATO. Three strains, labelled 9a (a predicted high affinity strain; an AAC deletion at 871bp in *lamB*), 19a (a frameshift mutant with non-functional LamB, T insertion at 610bp) and 62b (predicted low affinity strain; A $\rightarrow$ G at 1211bp) were identified with different maltotriose transport properties (Figure 3b), one-way anova, $F \approx 28.2, p < 7 \cdot 10^{-13}$). The three-strain version of (3) predicts they should coexist in a fluctuating resource environment, such as a batch culture, where bacteria are inoculated into fresh flasks each day with high initial resources that are depleted throughout a 24-hour cycle as the bacteria grow (Figure 4a).

We cultured 9a, 19a and 62b in DM with $300\mu g/ml$ of maltotriose for 18 days in such a batch culture microcosm and found, consistent with predictions, all three genotypes persisted. However, the model is not quantitative (Figure 4b): it fails to predict the relative frequencies at which each genotype was maintained. Most notably, the microcosm was dominated by the high-affinity strain, 9a, whereas the model predicts the low-affinity strain, 62b, should prevail (Figure 4a). This shows that consumer lifestyle and the between-strain RATO alone are not sufficient to explain the dynamics we observe.

To understand why theory and experiments disagreed, we reasoned that the RYTO could

play a role because it could lead fast-uptake genotypes to have low efficiencies which would impact growth rates. To justify this we followed the path of maltotriose through the cell which is converted to glucose and an excess of glucose produced at high maltotriose concentrations will lead glycolytic NADH to repress citrate synthase and, therefore, the TCA cycle.[29] As total ATP yield from the TCA cycle is greater per glucose supplied than from glycolysis, this repression should strengthen the within-strain RYTO we observed (Figure 1). We therefore included a glucose-dependent, maltotriose-to-biomass conversion efficiency into the model to mimic the RYTO (Supplementary Discussion, section D). Only then, with two trade-offs, do we have a theory consistent with the 18-day mean frequency dynamics of the strains that also exhibits the long-term coexistence of all three (Figure 4c).

To test for stable coexistence, we inoculated the three strains into a fresh microcosm at relative frequencies predicted by the trained dual trade-off model after running it to equilibrium. After so doing, we found no evidence of a deviation from the predicted strain frequencies when propagating them for a further seven days of seasonal co-culture (Figure 4c and Supplementary Discussion, section D). The eventual deviation that we observed of the microcosm from the theoretical prediction is only to be expected as the coexisting lineages likely gain further mutations that are not encoded within the model (Supplementary Discussion, section D).

Discussion

Trade-off shape is believed to be key to understanding species diversity in global ecosystems and our analyses concur. Our theoretical models and empirical analyses elucidate the shape of two, the RATO and RYTO. According to our theory, both must be invoked simultaneously to explain the stable maintenance of genetic diversity in an *E.coli* transporter gene, *lamB*, when mutants are co-cultured within a seasonal resource dynamic. The RATO, with its quadratic shape (Figure 3b), is the result of a biophysical constraint that arises because the transport of extracellular nutrients into the cell is optimised. As different transporter structures are optimal for different extracellular nutrient concentrations, a continuum of potential sugar uptake niches is created (Figure 4a) that here maintains

three genetic lineages. However, nutrient consumption alone cannot account for strain frequencies and differential efficiencies resulting from downstream metabolism due to the RYTO, with its sigmoidal shape (Figure 1c), ensure that efficient and not greedy consumers prevail.

Trade-offs have long been postulated as a mechanism supporting genetic diversity in ecosystems and it has become a fundamental problem in ecology to find them in living systems.[30] Importantly, we show they are predictable: because trade-offs are the result of physical processes within the cell, their shapes can be derived mathematically and corroborated against empirical data. Consistent with trade-off theories of biodiversity, we also show that polymorphisms in specific feeding genes are predictable. However, just one trade off was not enough, we need to account for the simultaneous presence of two to correctly predict allele frequencies in a bacterial microcosm. Therefore, theories of multiple simultaneous trade-offs[31] are likely needed to capture the diversity observed in natural ecosystems.

Methods

***lamB* mutant library generation**. We co-cultured *E. coli* strain B(REL606), from the laboratory of Richard Lenski, Michigan State University, Michigan, USA, with the obligatorily lytic λ strain cI26, from the laboratory of Donald Court, National Cancer Institute, Maryland, USA. When co-cultured with cI26, REL606 experiences strong pressure to evolve resistance because *E. coli B* strains lack generalized phage defenses such as mucoid cell formation, restriction modification, or CRISPR adaptive immunity.[32,33] This pressure is magnified by the lytic phages increased virulence as compared to its lysogenic relatives.[34] 100 flasks were initiated with 10^3 bacterial cells and even fewer phage ($\sim 10^2$ particles). We initiated the study with small populations to increase the likelihood that mutations for defense would arise *de novo*, which improved our chances of isolating unique *lamB* mutations. Culturing occurred in 50ml Erlenmeyer flasks, filled with $10ml$ of modified Davis Medium (DM)[35] ($125\mu g/ml$ maltotriose instead of glucose and $1\mu g/ml$ of magnesium sulphate), incubated for 24 hours, at 37^oC, and shaken at 120 rpm. Bacteria were pre-conditioned for a full 24-hour cycle before being co-cultured with phage. After

the first 24 hour of incubation in the mixed cultures, a random $100\mu l$ sample of each flask was transferred to a fresh flask and the bacteria and phage were allowed to grow again. This cycle was repeated twice and bacteria were sampled after the third day of growth. We ended the experiment at this early time-point to ensure that the bacteria only had enough time to evolve a single mutation for defense. Additionally, in previous experiments we observed the greatest genotypic diversity of bacteria on the third day. *E. coli* evolve resistance in this environment through mutations in many loci, however preliminary experiments revealed that *lamB* is the most common. For this study we focused just on genotypes that had mutations in *lamB*.

Bacterial isolation and storage. To isolate bacteria we streaked a sample on Luria Bertani (LB) agar plates,[36] incubated them for 24 hours at 37^oC, and arbitrarily picked two colonies. Next we re-plated each colony two more times serially to remove all phage. Finally we grew each colony in liquid LB overnight and preserved two 1ml samples in 15% glycerol and frozen at -80^oC. We tested whether each isolate had evolved resistance to λ by spot assay,[37] where $2\mu l$ of concentrated phage stock is dried on top of a matrix of 4ml of soft agar (LB agar with only 4% wv agar) and 0.5ml of the LB overnight culture. The matrix is suspended on top of a typical LB agar petri dish. Each plate was incubated at 37^oC for 24 hours and then scored the next day. A strain was considered resistant if no clearing occurred under the spot where the phage lysate was applied. We sequenced each of the resistant genotypes to determine if resistance had evolved through mutations in *lamB*.

Sequencing. Sequencing was performed with an automated ABI sequencer maintained at Michigan State University Research Technology Support Facility. PCR amplified fragments that were purified with GFX columns were used as templates. Fragments containing *lamB* were amplified with primer sequences 5′-TTCCCGGTAATGTGGAGATGC-3′ and 5′-AATGTTTGCCGGGACGCTGTA-3′, placed 1,398 bases up and 504 bases downstream of the *lamB* gene, respectively.

Growth dynamics. Each genotype was revived by inoculating a few microliters of frozen culture into a tube with 4ml of liquid LB. Cultures were grown at 37^oC and shaken at 160 rpm. After 12 hours, $10\mu l$ of each culture was transferred to a fresh tube with modified

DM 250 and grown for 12 hours at 37^oC and shaken at 160 rpm. This acclimation step to DM250 was repeated again because preliminary studies showed that growth was much more consistent when two sequential acclimation steps were preformed. Finally, $2\mu l$ of each culture (10^6 cells) was inoculated into a well with $200\mu l$ of modified DM. Wells were randomized in a 96-well plate, however cultures were never inoculated into the outer-rim to avoid edge-effects caused by increased rates of evaporation. Next the cells were incubated at 37^oC and the optical densities (at 420nm wave length) of each well was measured once every five minutes for 12 hours using a VersaMax automated plate reader (Molecular Devices). Each genotype was grown in modified DM supplemented with either $25\mu g/ml$ of maltotriose or $250\mu g/ml$, in four separate replicates. OD was converted into cell densities by comparing counts of colony forming units (CFUs) to optical densities at a number of different cell concentrations. Growth curves were created identically for the ancestor, REL606, except at many more concentrations of maltotriose (1, 2, 4, 8, 16, 32, 64, 128 $\mu g/ml$). These data were used to measure the RYTO.

Coexistence experiments. Coexistence experiments were run under the same conditions as the growth dynamics were measured, except maltotriose concentrations were increased to $333\mu g/ml$, plates were continuously shaken at 220rpm, and the experiments were run for 18 days by transferring a random sample of 2% of the culture after 24 hours of growth to a well with fresh medium. Coexistence was measured by tracking co-occurring populations of three genotypes; 9a, 19a, and 62b. To track the populations we used the *ara* genetic marker. Each of the three *lamB* mutant genotypes were unable to metabolize L-arabinose (*ara*-) because of a single nucleotide substitution in *araA* that caused a G-to-D amino acid change at position 92. We selected for spontaneous reversions of this mutation by growing $\sim 10^9$ cells of each strain on minimal arabinose plates for 48 hours at 37^oC.[35] Reversions were verified by targeted sequencing of *araA* using the same protocol for *lamB*, except the following primers were used for PCR amplification; 5′-CCGATACGCTCATGGGCTTGTTTA-3′ and 5′-CTGCCCAGGCCGTTGCGACTCTAT-3′. The *ara* genetic marker was chosen because previous work has shown that it does not confer a cost.[35] We cultured each *ara*+ genotype with the *ara*- version of the other two *lamB* mutants. The density of the focal genotype was measured by counting colonies on minimal arabinose plates. Total bacterial population size was also measured by counting colonies on LB plates. For each *ara*+ genotype we constructed four replicate populations

making twelve coexistence experiments in total.

References

[1] Maharjan, R. *et al.* The form of a trade-off determines the response to competition. *Ecology Letters* 1267–1276 (2013).

[2] Ben-Hur, E., Fragman-Sapir, O., Hadas, R., Singer, A. & Kadmon, R. Functional trade-offs increase species diversity in experimental plant communities. *Ecol Lett* **15**, 1276–1282 (2012).

[3] Kraaijeveld, A. R. & Godfray, H. C. Trade-off between parasitoid resistance and larval competitive ability in drosophila melanogaster. *Nature* **389**, 278–280 (1997).

[4] Fine, P. V. A. *et al.* The growth-defense trade-off and habitat specialization by plants in amazonian forests. *Ecology* **87**, S150–62 (2006).

[5] Leiby, N. & Marx, C. J. Metabolic erosion primarily through mutation accumulation, and not tradeoffs, drives limited evolution of substrate specificity in *Escherichia coli*. *PLoS Biol* **12**, e1001789 (2014). URL `http://dx.doi.org/10.1371%2Fjournal.pbio.1001789`.

[6] Friesen, M. L., Saxer, G., Travisano, M. & Doebeli, M. Experimental evidence for sympatric ecological diversification due to frequency-dependent competition in *Escherichia coli*. *Evolution* **58**, 245–260 (2004).

[7] Poelwijk, F. J., de Vos, M. G. J. & Tans, S. J. Tradeoffs and optimality in the evolution of gene regulation. *Cell* **146**, 462–470 (2011).

[8] Herron, M. D. & Doebeli, M. Parallel evolutionary dynamics of adaptive diversification in *Escherichia coli*. *PLoS Biol* **11** (2013).

[9] Fitzsimmons, J., Schoustra, S., Kerr, J. & Kassen, R. Population consequences of mutational events: effects of antibiotic resistance on the R/K trade-off. *Evolutionary Ecology* **24**, 227–236 (2010).

[10] Wong, W. W., Tran, L. M. & Liao, J. C. A hidden square-root boundary between growth rate and biomass yield. *Biotechnol Bioeng* **102**, 73–80 (2009).

[11] MacLean, R. C. & Gudelj, I. Resource competition and social conflict in experimental populations of yeast. *Nature* **411**, 498–501 (2006).

[12] Novak, M., Pfeiffer, T., Lenski, R. E., Sauer, U. & Bonhoeffer, S. Experimental tests for an evolutionary trade-off between growth rate and yield in *E. coli*. *Am Nat* **168**, 242–251 (2006).

[13] Pfeiffer, T., Schuster, S. & Bonhoeffer, S. Cooperation and competition in the evolution of ATP-producing pathways. *Science* **292**, 504–507 (2001).

[14] Gudelj, I. *et al.* An integrative approach to understanding microbial diversity: from intracellular mechanisms to community structure. *Ecol Lett* **13**, 1073–1084 (2010).

[15] Smith, S. L., Pahlow, M., Merico, A. & Wirtz, K. W. Optimality-based modeling of planktonic organisms. *Limnology and Oceanography* **56**, 2080–2094 (2011).

[16] Stewart, F. M. & Levin, B. R. Partitioning of resources and the outcome of interspecific competition: a model and some general considerations. *Am. Nat.* **107**, 171–198 (1973).

[17] Dethlefsen, L. & Schmidt, T. M. Performance of the translational apparatus varies with the ecological strategies of bacteria. *J Bacteriol* **189**, 3237–3245 (2007).

[18] MacArthur, R. & Wilson, E. *The theory of island biogeography* (Princeton University Press, 1967).

[19] Boos, W. & Shuman, H. Maltose/maltodextrin system of *Escherichia coli*: transport, metabolism, and regulation. *Microbiol Mol Biol Rev* **62**, 204–29 (1998).

[20] MacLean, R. C. & Gudelj, I. Resource competition and social conflict in experimental populations of yeast. *Nature* **441**, 498–501 (2006).

[21] Nikaido, H. & Vaara, M. Molecular basis of bacterial outer membrane permeability. *Microbiol Rev* **49**, 1–32 (1985).

[22] Saint, N. *et al.* Structural and functional characterization of ompf porin mutants selected for larger pore size. ii. functional characterization. *J Biol Chem* **271**, 20676–20680 (1996).

[23] Thirion, J. P. & Hofnung, M. On some genetic aspects of phage lambda resistance in e. coli k12. *Genetics* **71**, 207–216 (1972).

[24] Braun-Breton, C. & Hofnung, M. In vivo and in vitro functional alterations of the bacteriophage lambda receptor in lamb missense mutants of escherichia coli k-12. *J Bacteriol* **148**, 845–852 (1981).

[25] Heine, H. G., Kyngdon, J. & Ferenci, T. Sequence determinants in the lamb gene of escherichia coli influencing the binding and pore selectivity of maltoporin. *Gene* **53**, 287–292 (1987).

[26] Elbing, K. *et al.* Role of hexose transport in control of glycolytic flux in *Saccharomyces cerevisiae*. *Appl. Environ. Microbiol.* **70**, 5323–5330 (2004).

[27] Berezhkovskii, A. M. & Bezrukov, S. M. Optimizing transport of metabolites through large channels: Molecular sieves with and without binding. *Biophysical journal* **88**, L17–L19 (2005).

[28] Pagliara, S., Schwall, C. & Keyser, U. F. Optimizing diffusive transport through a synthetic membrane channel. *Adv Mater* **25**, 844–849 (2013).

[29] Stulke, J. & Hillen, W. Carbon catabolite repression in bacteria. *Curr Opin Microbiol* **2**, 195–201 (1999).

[30] Agrawal, A., Conner, J. & Rasmann, S. *Evolution After Darwin: the First 150 Years*, chap. Trade-offs and negative correlations in evolutionary ecology (Sinauer Associates Sunderland, MA., 2010).

[31] Doebeli, M. & Ispolatov, I. Complexity and diversity. *Science* **328**, 494–497 (2010).

[32] Spanakis, E. & Horne, M. T. Co-adaptation of escherichia coli and coliphage lambda vir in continuous culture. *J Gen Microbiol* **133**, 353–360 (1987).

[33] Daegelen, P., Studier, F. W., Lenski, R. E., Cure, S. & Kim, J. F. Tracing ancestors and relatives of escherichia coli b, and the derivation of b strains rel606 and bl21(de3). *J Mol Biol* **394**, 634–643 (2009).

[34] Lenski, R. E. Dynamics of interactions between bacteria and virulent bacteriophage. In Marshall, K. C. (ed.) *Advances in Microbial Ecology*, vol. 10, 1–44 (Plenum Press, New York, N. Y., 1988).

[35] Lenski, R., Rose, M., Simpson, S. & Tadler., S. Long-term evolution experiment in *Escherichia coli* 1. adaptation and divergence during 2,000 generations. *American Naturalist* **138**, 1315–1341 (1991).

[36] Sambrook, J. & Russell, D. W. *Molecular Cloning : A Laboratory Manual* (Cold Spring Harbor Laboratory Press, Cold Spring Harbor, New York, 2001), 3rd edn.

[37] Adams, M. *Bacteriophages* (Interscience Publishers, New York, 1959).

[38] Charbit, A. *et al.* *In vivo* and *in vitro* studies of transmembrane beta-strand deletion, insertion or substitution mutants of the *Escherichia coli* K-12 maltoporin. *Molecular Microbiology* **35**, 777–790 (2000).

Competing Interests

The authors declare that they have no competing financial interests.

Correspondence

Queries should be addressed to REB (r.e.beardmore@exeter.ac.uk) or JRM (jrmeyer@ucsd.edu).

Acknowledgements

The authors thank Chris Marx, Tom Ferenci, Christina Burch and other members of a NESCent working group 'Mathematical Models, Microbes and Evolutionary Diversification' for helpful discussions. We thank Richard Lenski and Donald Court for supplying bacteria and phage.

Figure 1: The RYTO shape can be derived from a simple branched metabolic pathway model and subsequently found in bacterial growth data. (a) A branched pathway predicts that cell yield, c, can be written in the form of equation (1) (derivation in Supplementary Discussion, section B). (b) As S_0 increases to 125$\mu g/ml$, r begins to saturate whereas k continues to increase. Moreover, two theoretical Monod models (light and dark grey) assuming, respectively, fixed and variable yield are both compatible with this (k, r) dataset. (b-inset) When S_0 ranges from 1 to $8\mu g/ml$, r and k appear linearly correlated, an observation consistent with published data[9] (error bars indicate mean $\pm$ s.e.m., horizontal s.e.m. bars are present but cannot be seen, 6 replicates per maltotriose concentration). (c) The variable yield model (equation (2)) was used to estimate rate-yield trade-off geometry: the solid line shows the predicted geometry using the dataset from (b), the dashed line improves on this prediction by fitting equation (2) directly to that dataset. (Supplementary Table 2 contains relevant parameter estimates.) Both of these trade-off models are sigmoidal, note, and the resulting predicted growth rate is shown as a dashed line in (b). (c-inset) A constant yield assumption fails when yield is plotted versus maltotriose concentration (light grey line). The nonlinear yield form from equation (1), $c(S_0)$, correctly captures the data (dark grey line).

Figure 2: The evidence for a between-strain RYTO is not significant at all maltotriose concentrations tested. (a) Estimated maltotriose uptake rate versus a robust estimate of cell yield (Supplementary Discussion, section C) for every genotype in the $lamB$ mutant library at two different maltotriose supply concentrations ($S_0 = 25$ and $250\mu g/ml$). Linear regressions show evidence of a between-strain negative correlation in yield but only when $S_0 = 250$ (error bars indicate mean $\pm$ s.d., $n = 8$; regression: $R^2 \approx 0.21$, F-statistic vs. constant model: $13.3, p < 0.00064$). (b) Ten strains from the library exhibit a feature common to all: although there are fluctuations due to experimental variation, cell yield is estimated consistently between strains across a range of maltotriose concentrations (error bars indicate mean $\pm$ s.e.m., $n = 3$; black and grey dots represent two different yield estimation algorithms, the horizontal dashed line is mean wild-type yield).

Figure 3: RATO data in the *E.coli* library is too noisy to discern a nonlinear shape, however a prior *Saccharomyces cerevisiae* dataset has a nonlinear RATO. (a) An indication the $E.coli$ library is consistent with a between-strain RATO: estimated values of K_m and $V_{\max}$ are positively correlated (error bars indicate mean $\pm$ s.e.m., $n = 8$). (b) Maximum likelihood estimates of $(K_m, V_{\max})$ for library strains 9a, 19a and 62b showing approximate 70% and 95% confidence contours of marginal posterior distributions determined using the Matlab MCMC Toolbox (MLEs of K_m in mM units: $0.011mM, 0.080mM$ and $0.211mM$, respectively. As a comparison, $E.\ coli$ strains from the literature[38] have values around $0.4mM$). (b-inset) Using this data, library strains were isolated (9a, 19a and 62b) that exhibit a between-strain RATO (see anova in main text). (c) A whole cell $S.\ cerevisiae$ $(K_m, V_{\max})$ dataset (mean data and standard error bars from[26]) exhibits a nonlinear uptake-RATO. Two robust geometric datafits are shown next to the robust linear regression $\mathsf{K_m = a + bV_{max}}$: a near-quadratic power law, $\mathsf{K_{m,p}}$, and a rational function, $\mathsf{K_{m,r}}$. Relative likelihoods of the two nonlinear fits indicate both are significantly better descriptors of the data than a linear function (the indicated $\mathsf{RL_{linear}}$ values are the relative likelihoods for each fit). This demonstrates consistency between the predicted nonlinear RATO shape (equation (5)) and data.

Figure 4: As predicted by population genetics theory, three *lamB* mutant strains can be stably co-maintained in a laboratory microcosm. (a) A theoretical three-strain co-culture model ($N = 3$ in a seasonal extension of equation (3)) containing a RATO but no RYTO predicts strain dynamics for 18 days when maltotriose is supplied each day at 300$\mu g/ml$. Maltotriose uptake rates, affinities and yields were estimated for each strain in monoculture and the inset shows estimated growth rate for every library strain: strains 9a, 19a and 62b are predicted to have fastest growth in different maltotriose concentration windows. (b) While the model correctly predicts the co-maintenance of three strains, this was not at the strain frequencies that were subsequently observed. Note, 62b has mean population size on day 18 of over 1 million cells (colony-forming units (CFUs)) despite a mean relative frequency of 2.4% (error bars indicate mean $\pm$ s.e.m., $n = 3$). (c) A RYTO was then introduced into the model that was used to make the predictions in (a) and the resulting model is consistent with strain frequencies (Supplementary Discussion, section D). One model simulation is shown (thick lines) superimposed upon observed mean strain frequencies (dots). (c-inset) The internal complexity of the $E.coli$ strains on which simulations in (c) are based, assuming only polymorphisms in $lamB$. (d) The three strains were co-cultured anew in the same conditions but this time they were inoculated at the model-predicted steady state frequencies, these frequencies were then maintained for a period of seven days (Supplementary Discussion, section D). Mean observed frequencies are shown next to the model predictions in (c) by the label 'extension', the observed densities of this extension are shown in (d). Note: numerical text labels in each plot indicate relative frequencies of each strain.

BIOPHYSICAL MECHANISMS THAT MAINTAIN BIODIVERSITY THROUGH TRADE-OFFS

R. E. BEARDMORE, I. GUDELJ, AND J. MEYER

Notation: throughout we use a minuscule 'k' for carrying capacity, whereas majuscule K and K_m are synonymous and represent a half-saturation constant, V and $V_{\max}$ are also used synonymously for maximal uptake rate.

Contents

Supplementary Figures

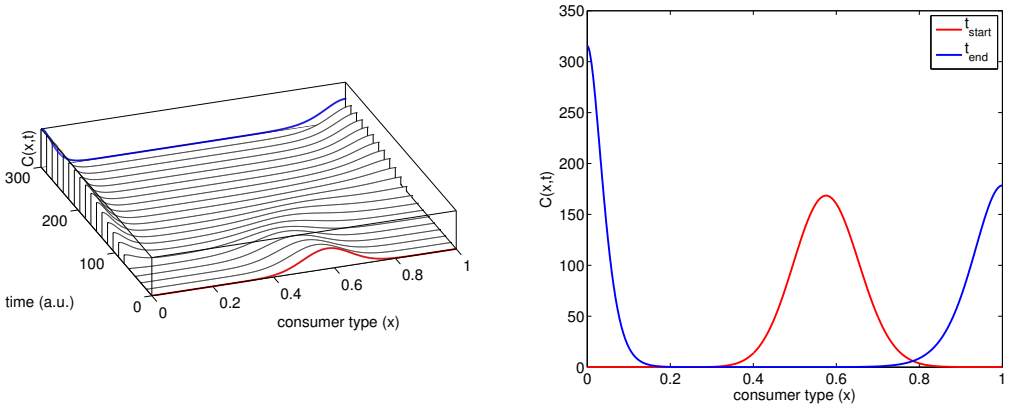

Supplementary Figure 1 – Evolutionary branching in equation (1) for the concave trade-off function $\tau(x) = 1 - x^{1/2}$. The initial distribution of consumers (in red when $t = t_{\text{start}}$) is an approximately normal distribution obtained by finding a steady-state of (1) for the concave trade-off function $\tau(x) = 1 - x^2$. The final distribution of consumers, after branching, is shown in blue (where $t = t_{\text{end}} \gg t_{\text{start}}$).

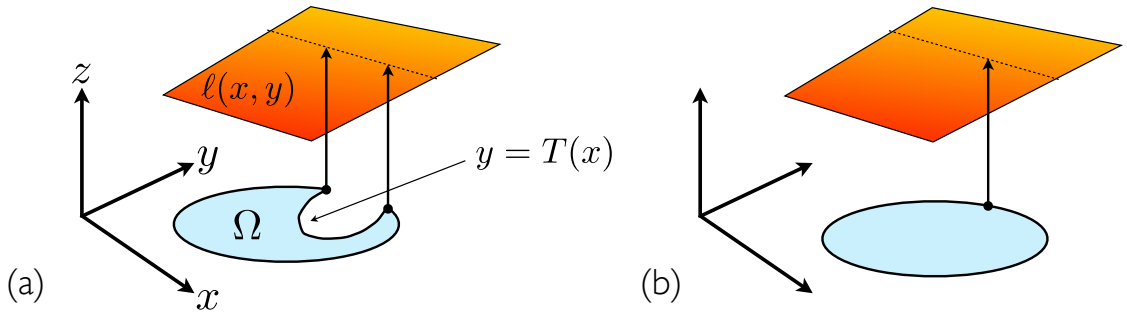

Supplementary Figure 2 – Finding the yellowest points on the plane above a point within Ω. The optimum of a linear functional, $\ell(x, y)$ over two different domains, Ω, in both cases must lie on the boundary of the domain. Only in case (a) does the possibility exist for two simultaneous solutions to the optimality problem. In case (b) where the region Ω is strictly convex, there is a unique maximum of ℓ.

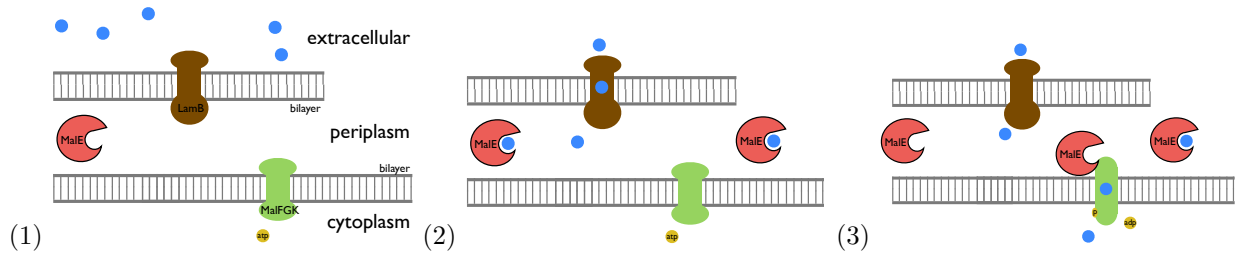

Supplementary Figure 3 – A schematic of how maltotriose enters the cytoplasm. The uptake of a sugar like maltotriose in Gram negative bacteria requires the molecule to pass two transporters positioned in serial (LamB and MalFGK_2) via a maltotriose-binding protein (MalE) before entering the cytoplasm. Transport through the inner-membrane transporter, MalFGK_2, requires an ATP-driven conformational change, a biological feature that we neglect from the mathematical assumptions in this article.

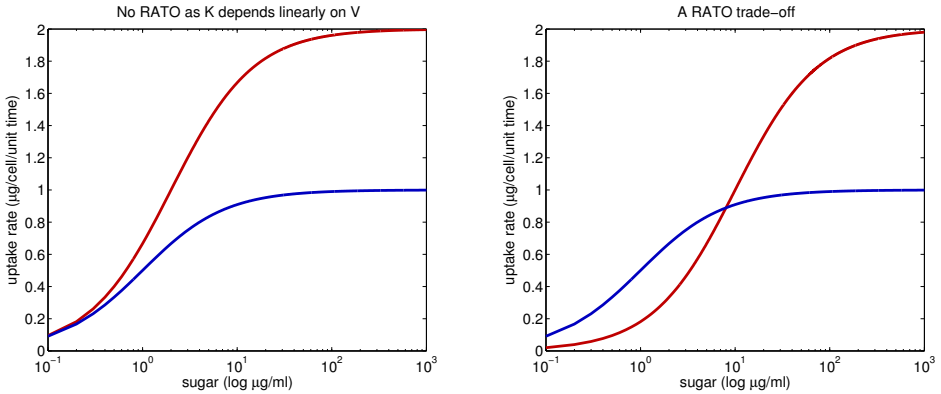

Supplementary Figure 4 – The presence of a nonlinear (and not linear) rate-affinity trade-off can lead to the right growth rate responses needed for strain coexistence. (left) The uptake of an extracellular sugar for two different cells (one red, one blue) at a range of external sugar concentrations on a semi-log scale. Here, there is no rate-affinity trade off even though there is a linear relationship between maximal uptake rate V and half-saturation constant K. Thus, it is the cell associated with the red curve that is fitter than the blue in all environments, independently of their resource richness. (right) In this case there is a rate-affinity trade-off in these two cells: the cell with the greatest maximal uptake rate V has a higher uptake rate at high-sugar environments, but that gain is paid for by a decrease in uptake at low sugar concentrations. In this case, it is possible that both cell phenotypes can coexist in an environment where sugar concentrations oscillate regularly between high and low values.

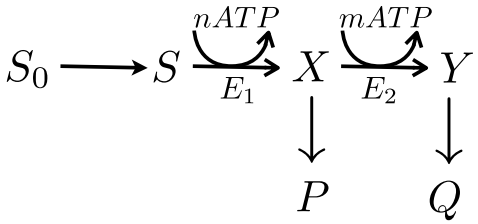

Supplementary Figure 5 – An internal sugar (S_0) is processed by a two-step pathway with a single branch; this structure is sufficient to derive the shape of a rate-yield trade-off. Each step has a different ATP yield and the shorter pathway has yield n, the full pathway has yield $n+m$ where $n < m$. If we define yield as the ATP produced per X produced per unit time in steady-state, we will show that this model exhibits a rate-yield trade-off.

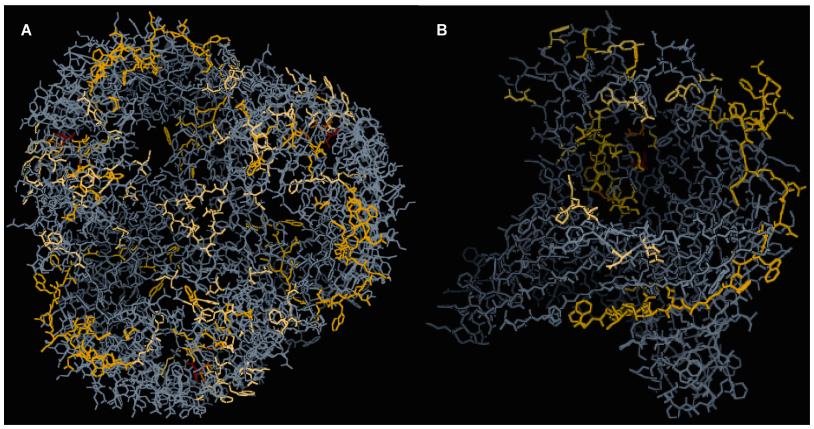

Supplementary Figure 6 – The distribution of all the mutations found in the *lamB* mutant library has been projected onto the three-dimensional conformation of LamB. Each panel provides a different perspective of the same protein relative to the membrane. A is the view from outside of the cell, the membrane follows the plane of the page. B is a view of structures that bisect the membrane, which would project horizontally from the page. A colour spectrum from yellow to red was used to indicate the frequency of mutations observed at each amino acid; yellow = 1 through red = 5, gray = 0.

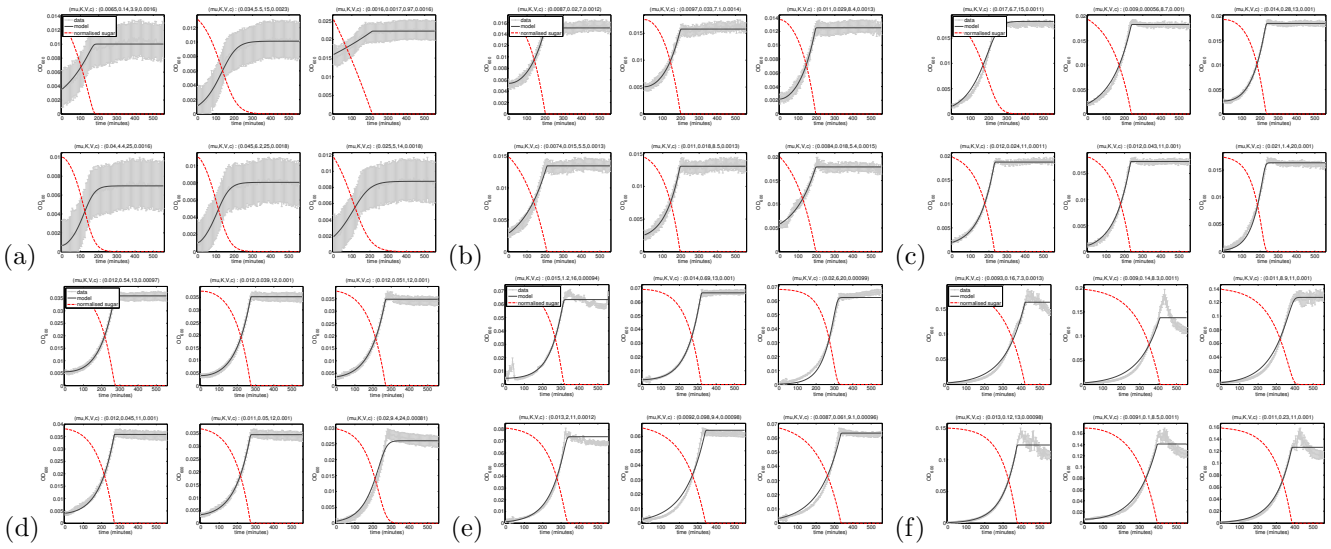

Supplementary Figure 7 – Wild type *E.coli* B(REL606) growth data showing fits of the mathematical growth model (21) to experimentally-determined density data determined over 24h. Shown are the results of using eight different resource (maltotriose) supply concentrations: $S(0) = 4^{(a)}, 8^{(b)}, 16^{(c)}, 32^{(d)}, 63^{(e)}, 125^{(f)} \mu g/ml$, (6 replicates per concentration, plots for $S(0) = 1$ and 2 are not shown). Error residuals only use data up to 550 mins, the x-axis denotes the length of the experiment in minutes (vertical bars indicated mean ± s.e., n=6). The red lines are normalized sugar concentrations, indicating when stationary phase is estimated to begin in the theoretical datafits.

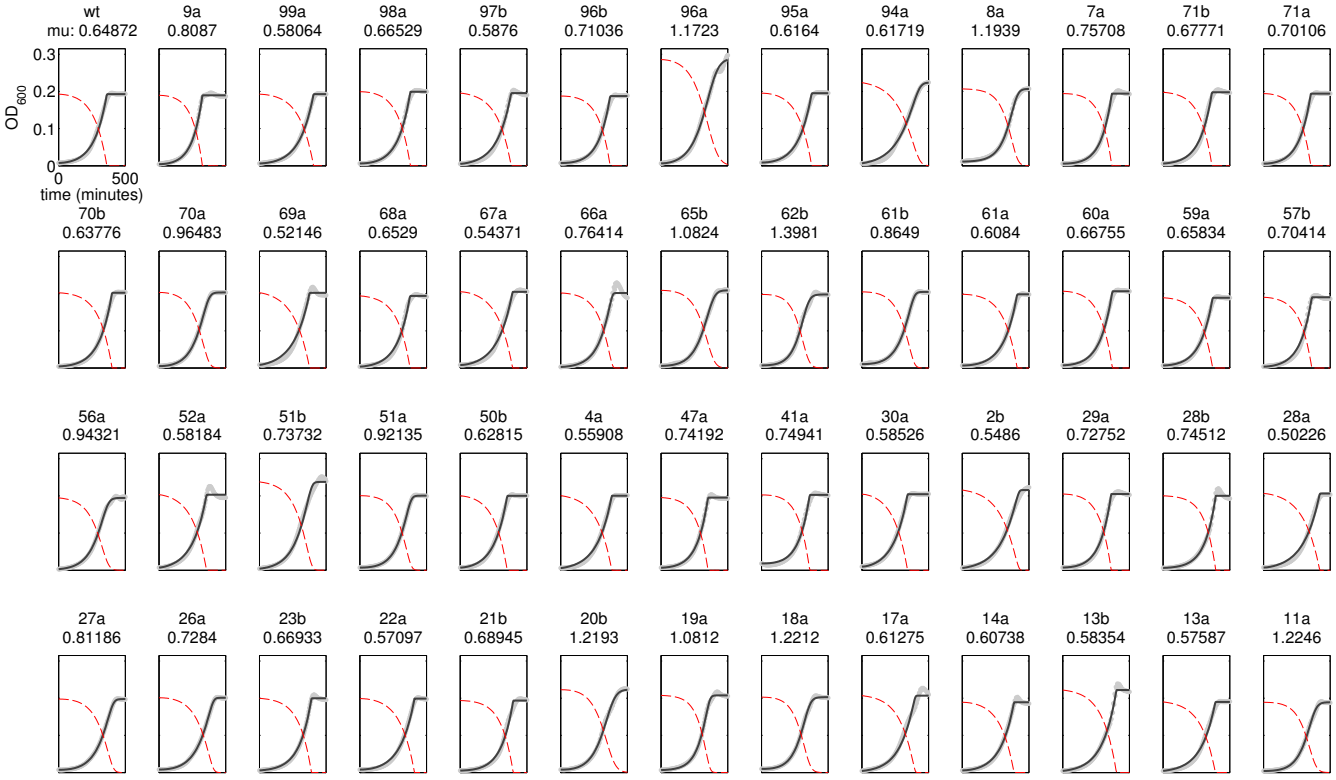

Supplementary Figure 8 – Datafits for the library of fifty-two strains used to to determine (c_j, K_j, V_j, ν_j) for each bacterial genotype. These were obtained by fitting a mathematical model, equation (21), against 24h growth data under maltotriose limitation (here using initial concentration $250 \mu g/ml$). No fit has an adjusted R^2 lower than 0.99. The red line denotes normalized maltotriose concentration for the datafit, showing an estimate of stationary phase.

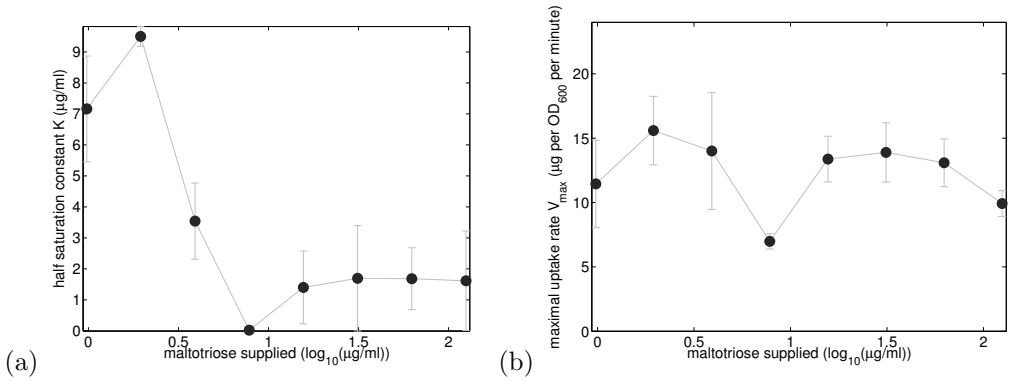

Supplementary Figure 9 – Datafits shown in Supplementary Figure 7 produce 42 independent estimates of the maximal maltotriose uptake rate, V_0, and the half saturation constant, K_0 for the wild type (the strain $j = 0$). (a) The variability of K_0 both between replicates and at different sugar supply concentrations. (b) The variability of V_0 from different fitting operations (error bars indicate mean ± s.e., n = 6).

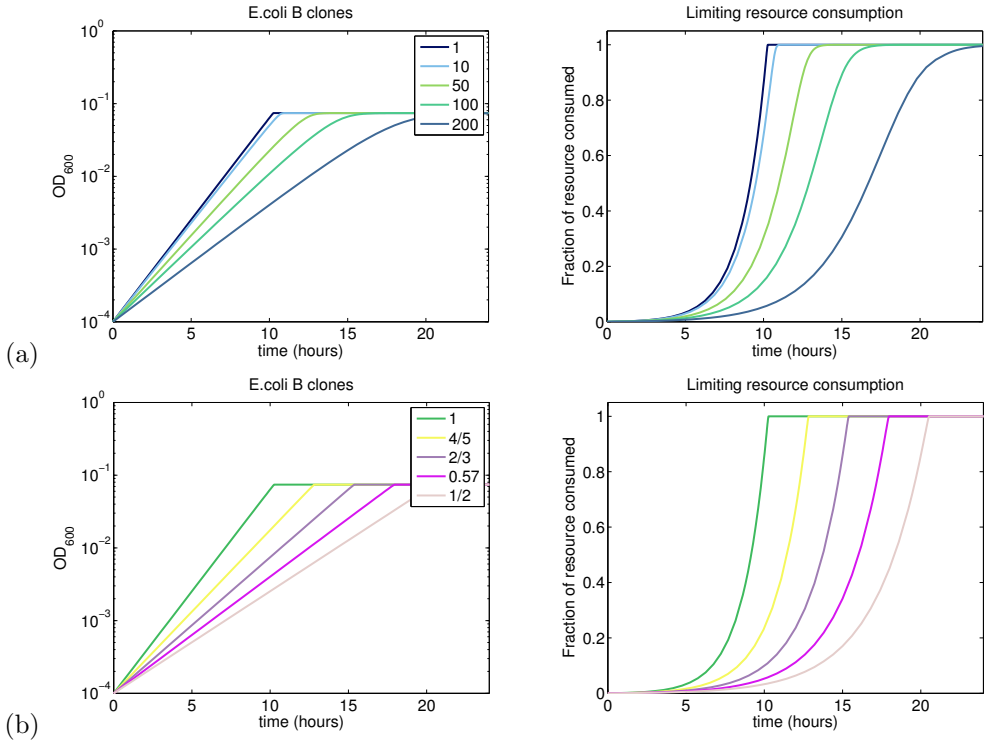

Supplementary Figure 10 – How changes in V and K affect the theoretical growth kinetics of a single bacterial strain. (a) Predicted growth kinetics of five hypothetical *E.coli* strains at a maltotriose supply concentration of $100\mu g/ml$ where the value of K for each strain has been obtained by scaling a basal value of K by the number shown in the legend of each plot, assuming that basal value to be $K \approx 0.4\mu g/ml$. The latter has been multiplied by the number in the legend (**greater than unity**) to produce a value of K for the simulated model. Thus, these five modelled strains have identical metabolic parameters except that K ranges from $0.4\mu g/ml$ to $50\mu g/ml$. (b) An analogous plot to (a) except that K is now held fixed and the parameter V has been scaled by a value **less than unity** shown in the figure legend to produce growth kinetics for five theoretical strains: note how the effects of varying K and V on these growth curves are visually different, although both affect observed growth rate. These differences arise because these two parameters are linearly independent in the data-fitting procedures and mathematical models used in this article. This figure also shows that K and V play reciprocal roles in those datafits: increasing K has the opposite effect on modelled growth rate to increasing V.

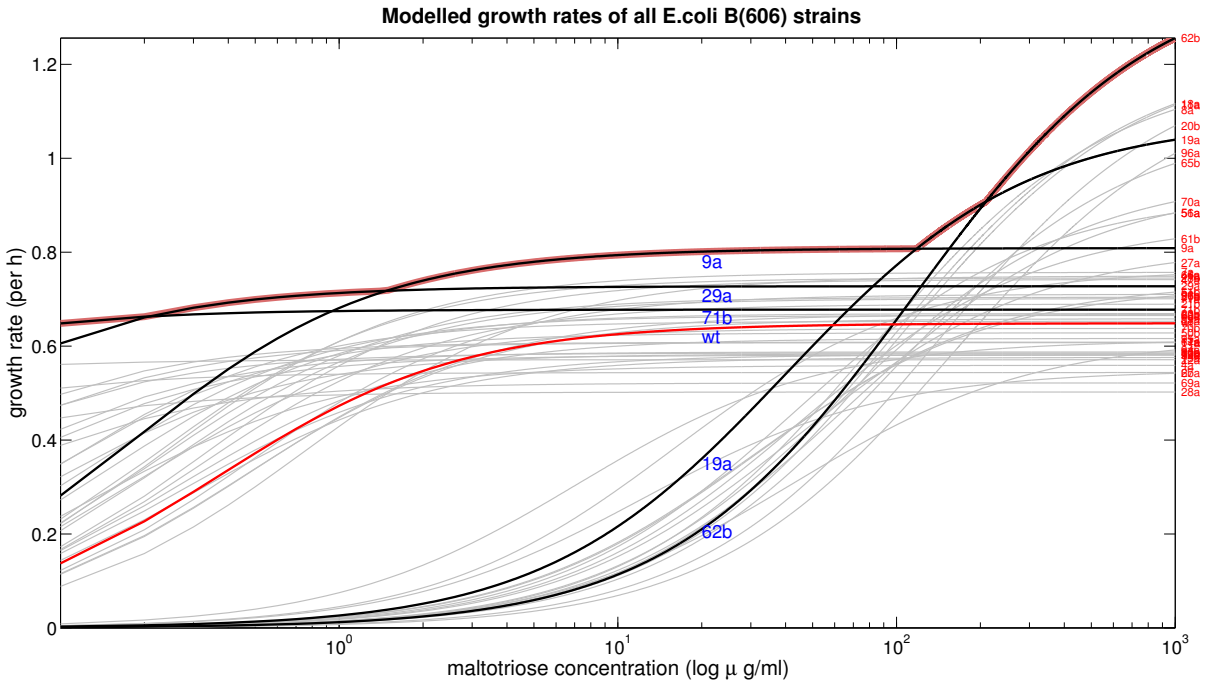

Supplementary Figure 11 – Theoretical predictions of growth rate on the y-axis plotted versus maltotriose concentration on the x-axis (one black growth rate curve per *lamB* mutant). This indicates that the bacterial library may have two clusters, one with a low but stable growth rate at all maltotriose concentrations and one with a high maltotriose affinity but the potential for low growth rate. The wild-type (shown in red) appears to be optimized for neither of these traits as it resides at the boundary of the two clusters. Strains with the highest growth rates at some point along the resource gradient are highlighted in blue text. It is instructive to compare the similarities of this figure with Supplementary Figure 4.

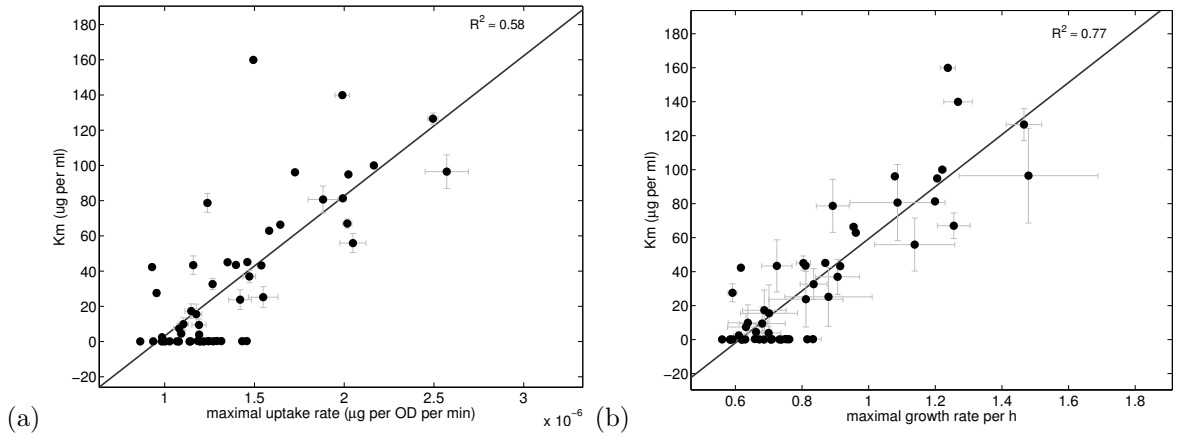

Supplementary Figure 12 – In search of a RATO: plots of uptake rate and growth rate versus K_m for each strain in the mutant library showing a noisy correlation but no clear evidence of 'shape'. A scatter plot of *all* the estimated values of (K_j, V_j) for all the strains where error bars show the variability when data fits are conducted using different lengths of time, the values of which are defined in the text. (b) This is the analogous plot to (a) except the data $(K_j, \mu_{\max_j})$ is shown where j takes on all 52 values, one for each strain (error bars indicate mean ± s.e., n = 7). The data is too noisy to resolve a RATO shape.

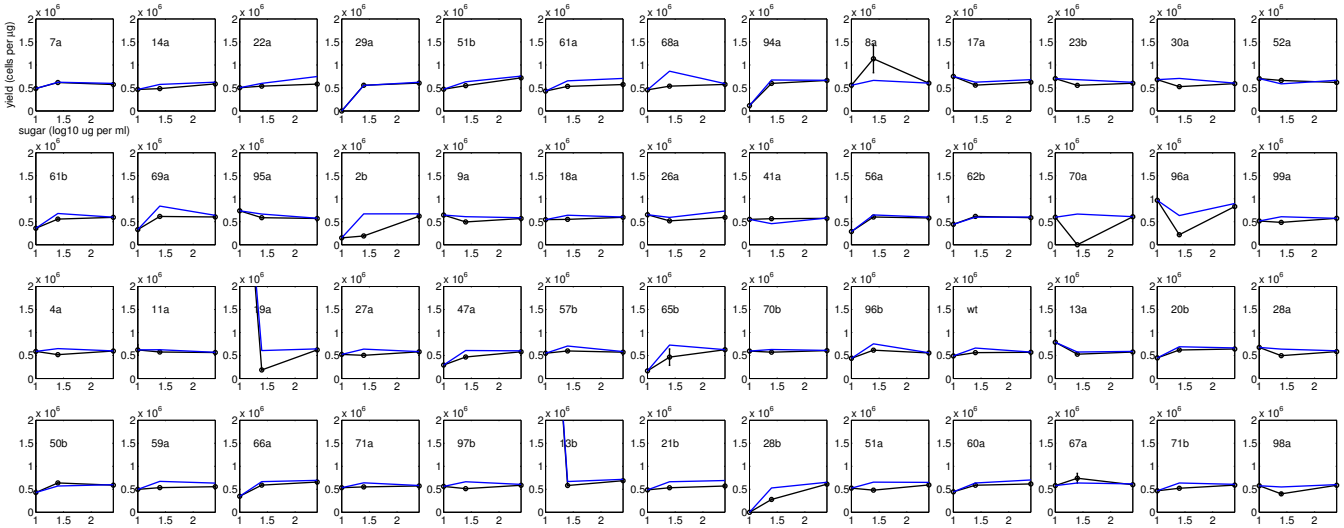

Supplementary Figure 13 – Two different versions of cell yield (the 'robust' yield in blue, the 'naive' yield in black) determined for three different sugar concentrations: $S(0) = 10, 25$ **and** $250\mu g/ml$. While there are some anomalies in the data where a value of zero has been reported (strains 29a, 70a, 28b) due to a poor datafit, this data shows no evidence of a reduction in per maltotriose yield at higher maltotriose concentrations. Moreover, there are no significant differences in yield between strains, note also that the robust and naive yield provide similar values in almost all cases (error bars are s.d., n=3).

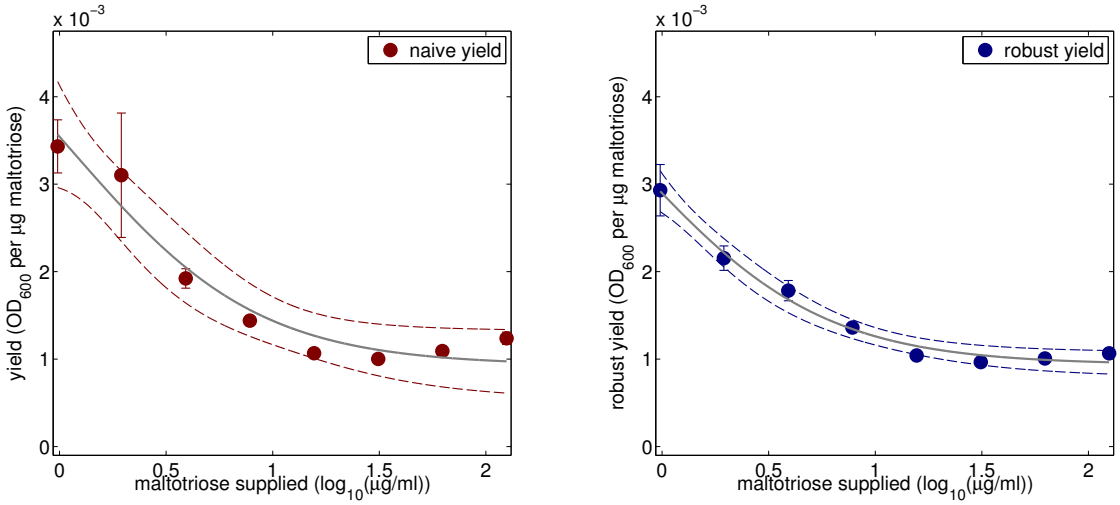

Supplementary Figure 14 – 'Naive' and 'robust' estimates (left and right respectively) of yield per μg **of maltotriose for the wild-type** *E. coli* **(REL606) strain are both well-described by the functional form in equation (20)**. There is a reduction in yield by a factor of approximately three as maltotriose ranges from 1 to $10\mu g/ml$ (error bars indicate mean ± estimated s.e.).

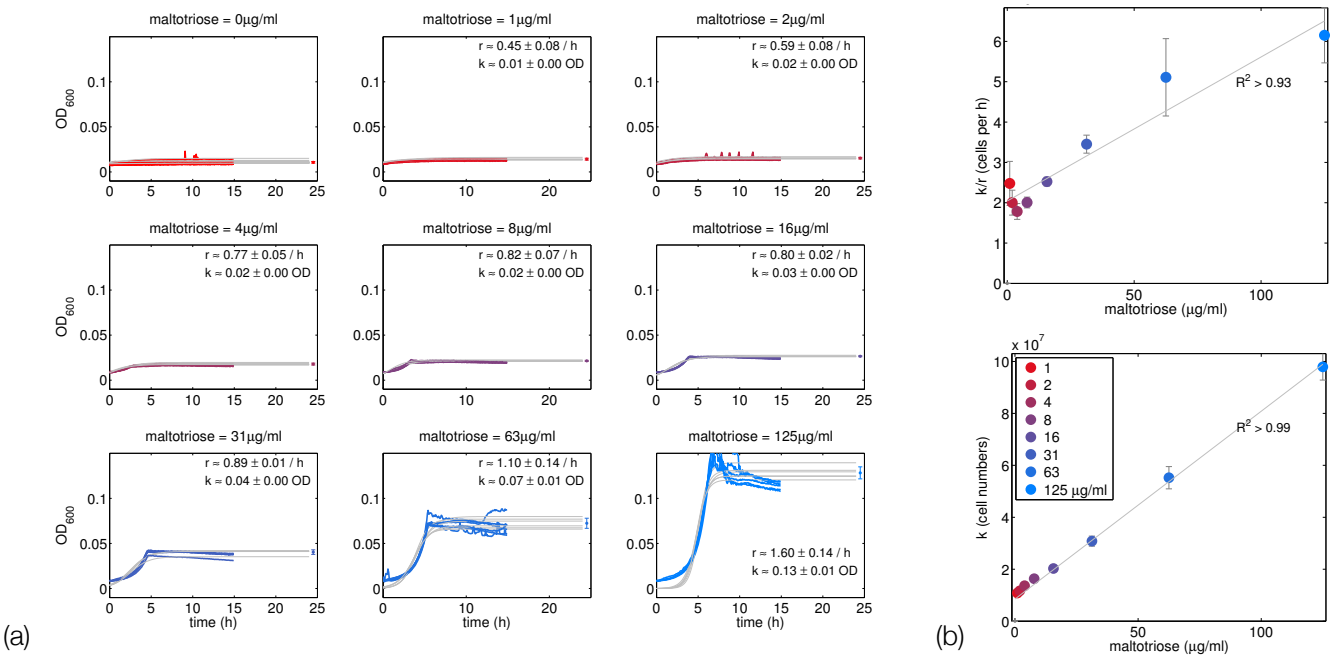

Supplementary Figure 15 – Experiments to estimate the values of r (growth rate) and k (carrying capacity). (a) Estimating r and k parameters by fitting a solution of the logistic equation, $\frac{d}{dt}x = rx(1 - x/k)$ to optical density data (where $x = \mathsf{OD}_{600\mathrm{nm}}$). The value of r is given as text within the plot and the value of k is represented as a colored vertical bar in each pane that shows the mean k estimate ± s.d. (six replicates). (b) (left) A linear correlation between k/r and S_0 where eight different values of the latter have been used, from 1 to $125\mu g/ml$. (right) A linear correlation between k and S_0 (error bars denote s.d.)

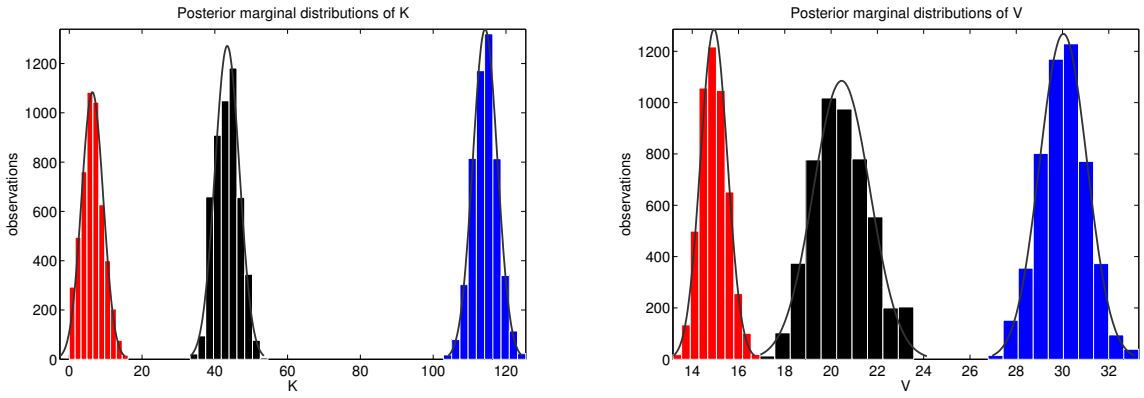

Supplementary Figure 16 – Histograms that illustrate posterior marginal distributions of K and V for strains 9a, 19a and 62b as determined using the Matlab MCMC Toolbox (5,000 points per strain) applied to (21) (normal distributions have been superimposed). This shows a positive rate-affinity correlation for these strains. **Comment**: the *E. coli* strains described in [1, Table 2] have maltotriose half saturation constants around $0.4mM$, the data presented in this figure gives approximate maximum likelihood values of $0.011mM$, $0.080mM$ and $0.211mM$ for strains 9a, 19a and 62b, respectively. Respective estimates for the maximal uptake rates in units of μg per cell per hour are $1.16 \times 10^{-6}\mu g \cdot h^{-1}\cdot$ per cell, $1.70 \times 10^{-6}\mu g \cdot h^{-1}\cdot$ per cell and $2.32 \times 10^{-6}\mu g \cdot h^{-1}\cdot$ per cell.

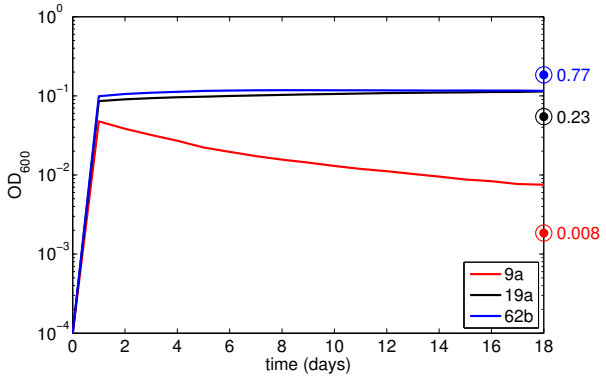

Supplementary Figure 17 – A theoretical prediction using data on the strain library: stable coexistence is possible for three different lamB mutants (9a, 19a and 62b) at $S_0 = 300\mu g/ml$. The circles mark steady-state values, for clarity density dynamics are only shown for 18 days.

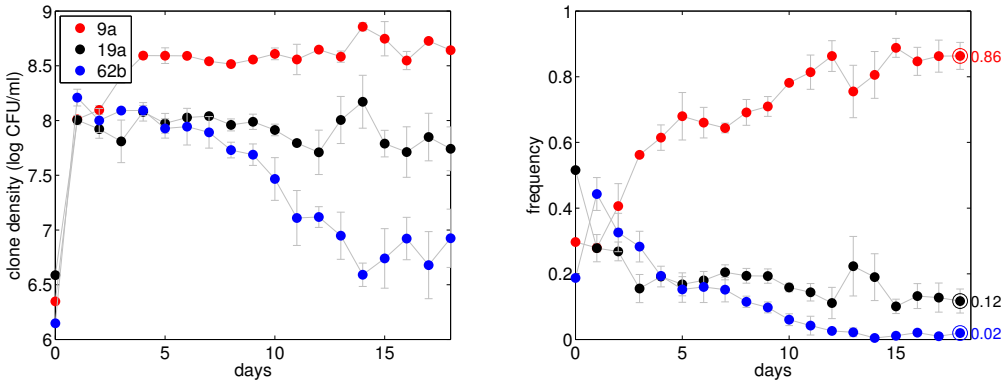

Supplementary Figure 18 – Strain densities and frequencies of the co-culture microcosm, implemented for 18 days. Competition of three clones under maltotriose limitation when this carbon source is supplied at $333\mu g/ml$ to a seasonal, batch-transfer microcosm (with 24 hours per season) in which the three strains of *E. coli* B(REL606), labelled 9a, 19a and 62a, are co-cultured for 18 days, approximately 130 generations. The left-hand figure shows densities (in log CFUs) the right-hand figure shows frequencies (error bars indicate mean ± s.e., n = 3).

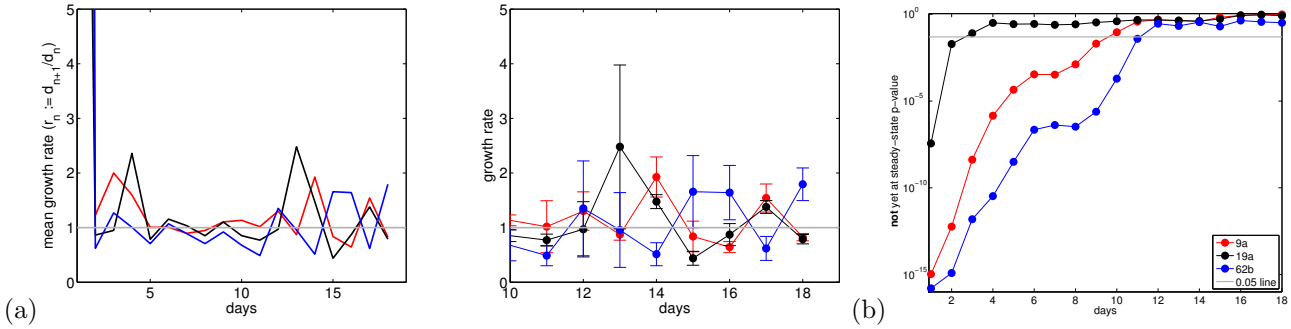

Supplementary Figure 19 – Testing for co-maintenance in the co-culture microcosm. The 'transfer-to-transfer growth rate' of each of each strain is defined as $r_n := d_{n+1}/d_n$ where d_n is the density of that strain on day n so that $r_n \equiv 1$ in steady-state. The left-hand plot illustrates mean growth rate: a high initial growth rate follows the inoculum, then a decline which subsequently oscillates about unity. The right-hand plot shows the dynamics with error bars (indicating mean ±s.e., n = 3). (b) When any of the three curves are below the grey line, the dynamics are not yet in steady-state according to a one-way anova at the $p = 5\%$ significance level described in the text.

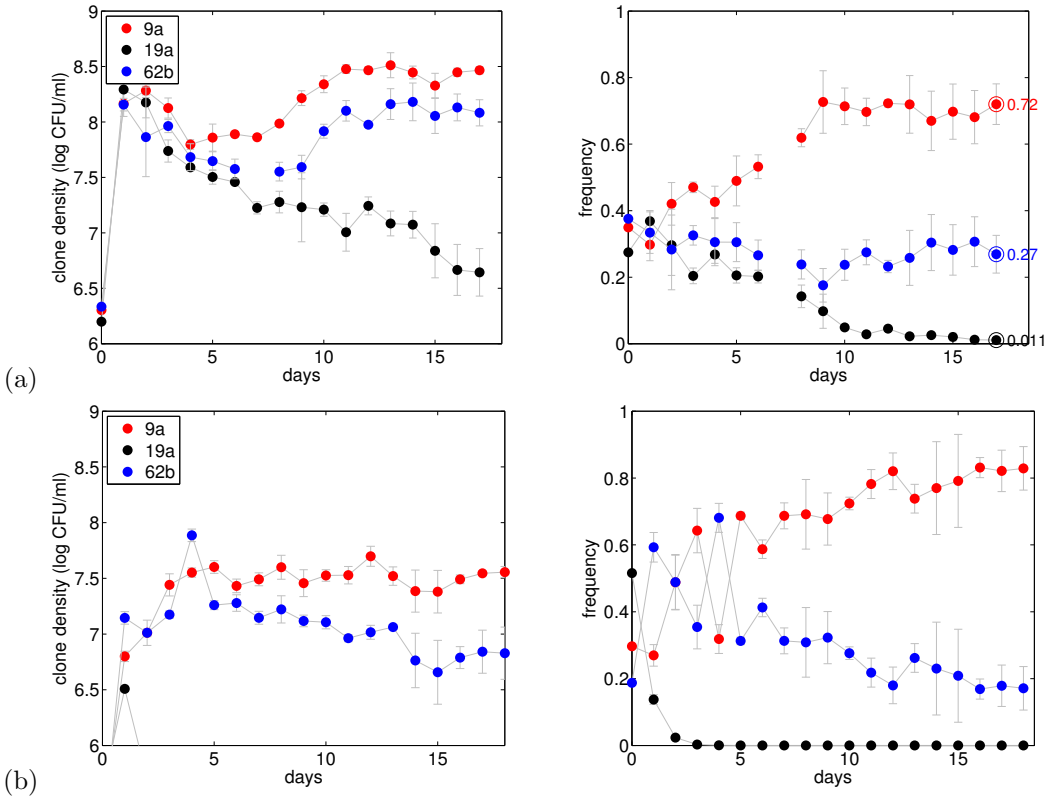

Supplementary Figure 20 – Do all three coexisting strains also coexist if the microcosm is implemented in a different way? No. (a) The analogous data to that shown in Supplementary Figure 18 except that a season length of 12h has been used, note how 19a decays in frequency (error bars indicate mean ± s.e., n=3). (b) This is also analogous to Supplementary Figure 18 except that maltotriose supply has been reduced to $33\mu g/ml$ and strain 19a is lost exponentially quickly.

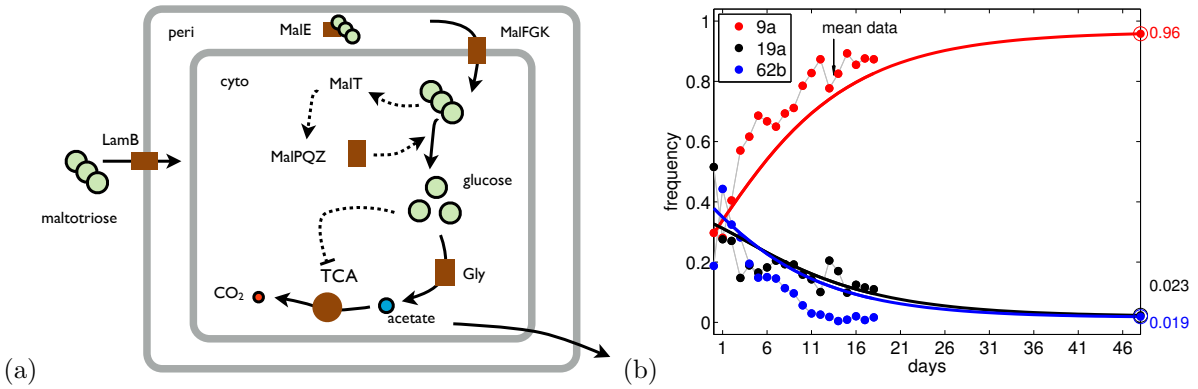

Supplementary Figure 21 – Predicting the relative frequencies of the three strains from a mathematical model based on the function of key genes. (a) A schematic of the metabolism of *E.coli* used as the basis of a mathematical model defined by equations (26). The import of an external sugar into the cell can lead to fast but inefficient growth due to the suppression of efficient, but slower, pathways. (b) Frequency dynamics of observed data (only the mean is shown) and of one instance of the model (26) parameterized using data from Supplement table 1 and Supplementary Figure 19. This establishes that the model is both consistent with the observed strain frequency dynamics and that all three strains co-exist in equilibrium in that model.

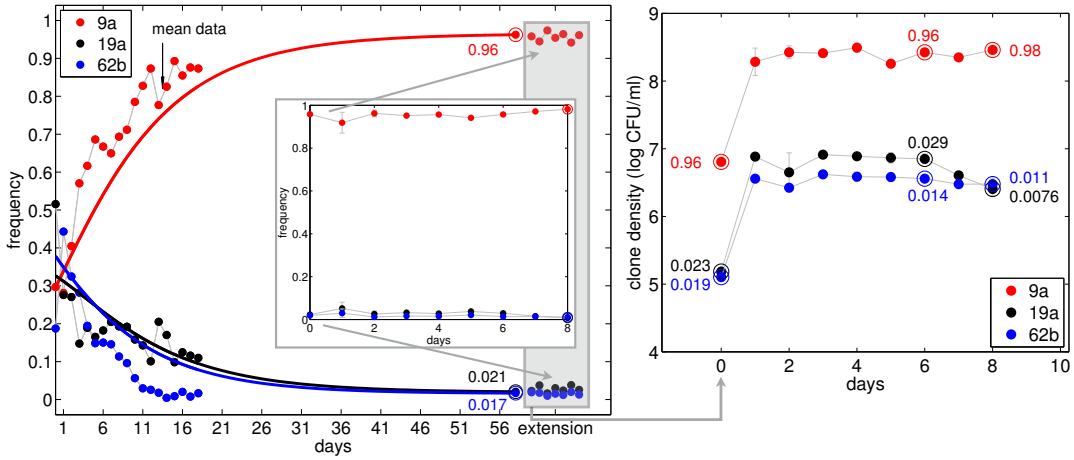

Supplementary Figure 22 – Implementing the co-culture microcosm, but now starting at the theoretically predicted long-term strain frequencies. An extension of the experiment used to produce the data for Supplementary Figure 19 that was obtained by setting the relative frequencies of the three strains to the equilibrium values predicted by the mathematical model (26)(a-f) and shown at the right-hand extreme of the plot in Supplementary Figure 21(b). The coloured numerical values used throughout this figure indicate relative strain frequencies and the right-hand plot shows strain densities. The inset of the left-hand figure appears to indicate constancy of the frequencies for 8 days, a statistical test described in the text shows that this constancy can only be claimed to be significant for 7 days.

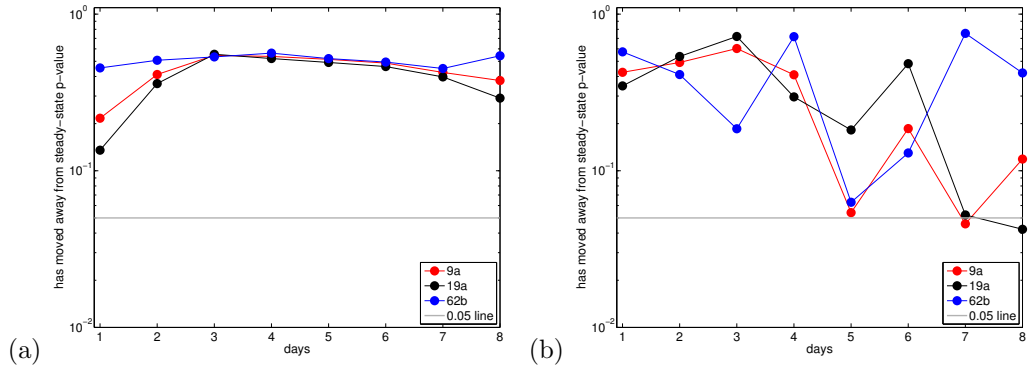

Supplementary Figure 23 – Two tests for constancy of the empirical strain frequencies through time. (a) A test based on the serial application of one-way anova (described in the text) cannot detect differences between the mean frequencies of any strain through time even at significance well above the 5% level (note how none of the curves cross the grey line). (b) If we perform a t-test that asks if the latest observed strain frequencies are, for any strain, different from the starting frequencies then this particular test fails at the 5% level on day 7. We can therefore claim significant equilibrium dynamics of all three strain frequencies for 7 days, but no longer.

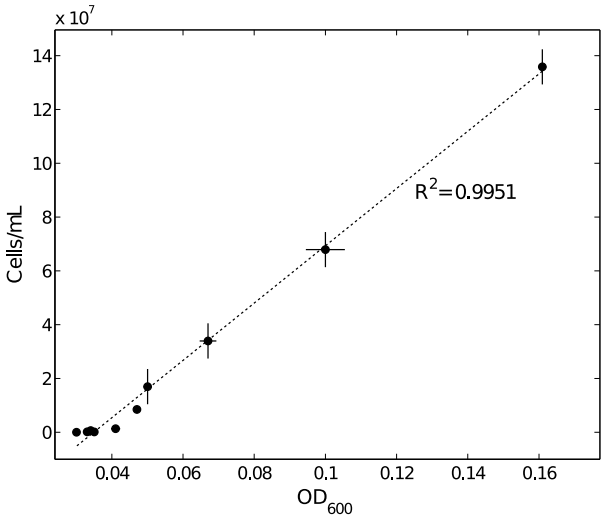

Supplementary Figure 24 – Are CFU and OD equivalent measures of population density? Yes, provided population density is high enough. Validation that *E.coli* cell densities as measured in units of OD or CFU are approximately equivalent, we deduce that 10^9CFU per ml $\approx$ 0.26OD.

Supplementary Tables

Supplementary Table 1 – *E.coli* B(REL606) mutants derived from a wild-type strain following coevolution with λ-phage, showing their library identifier and the mutations found in *lamB*. The right-hand column shows a typical dataset produced by fitting the mathematical growth model (21) to the library at one maltotriose concentration. The values for each genotype are: c_j is yield in units of OD per μg, K_j is half saturation in $\mu g/ml$, V_j in μg per OD per minute and ν_j is quoted per minute. Maximal growth rate per hour, therefore, is $\mu_{\max_j} = c_j \times V_j \times 60$ in per hour units. For example, the wild-type yield on maltotriose is estimated as $5.9{\times}10^5$ cells/μg with maximal uptake parameter $V_0 \approx 1.1 \times 10^{-6} \mu g$ per wild-type cell per hour from 14.6 per OD/min.

label	**mutation found** (SNP unless stated otherwise)	**location on** *lamB* (b.p.)	c_j	K_j	V_j	ν_j
wt ($j = 0$)	N/A		0.00074	0.37	14.6	0.0076
2b	deletion: -GAC	292-294	0.00084	12.2	10.9	4.6
4a	C → A	854	0.00078	0.14	11.9	0.18
7a	insertion: +TCGCAGGGTAAAGGGCTG	795-796	0.00075	0.24	16.7	0.0055
8a	-GATTTCAA	1264-1271	0.00078	81.4	25.4	0
9a	-AAC	871-873	0.00074	0.18	18.2	0.014
11a	T → G	556	0.00074	99.9	27.5	0.0040
13a	+TACGGTCGTGCCAACTTGCGTGATAACT	652-653	0.00074	0.3	12.9	0.41
13b	-GCCGTTCCTGCTGATTTCAA	1252-1271	0.00087	0.081	11.1	0.62
14a	T→ G	835	0.00073	0.028	13.8	0.015
17a	-AAC	871-873	0.00081	7.17	12.6	8.0
18a	T → G	538	0.00077	93.9	26.3	0.0026
19a	+T	610-611	0.00080	40.0	22.4	0
20b	-A	349	0.00086	140.0	23.5	0.0050
21b	+TCGCAGGGTAAAGGGCTG	795-796	0.00075	0.3	15.2	0.0041
22a	G → T	1210	0.00076	0.001	12.4	0.0092
23b	A → C	793	0.00078	0.14	14.3	0.00010
26a	-AAC	871-873	0.00077	30.0	15.7	0.0065
27a	+T	597-598	0.00076	43.4	17.7	0.0055
28b	-T	726	0.00079	0.012	10.5	0.039
29a	A → G	518	0.00079	0.02	15.3	0.0040
30a	G → A	571	0.00078	0.02	12.5	0.024
41a	A → C	284	0.00074	0.75	16.9	0.0017
47a	T → A	850	0.00075	0.33	16.3	0.0030
50b	G → T	874	0.00077	0.080	13.5	0.015
51a	C → A	824	0.00077	43.2	19.8	0.0039
51b	C → A	843	0.00093	31.1	13.1	5.2
52a	G → T	809	0.00078	0.2	12.3	0.076
56a	-AAAGGGCTGTCGCAGGGT	805-822	0.00077	66.9	20.4	2.2
57b	C → T	788	0.00075	0.22	15.7	0.037
59a	G → C	1285	0.00073	0.47	15.0	0.0056
60a	G → T	709	0.00080	0.49	13.9	0.0062
61a	A → C	518	0.00077	0.02	13.2	0.0069
61b	G → T	559	0.00078	43.8	18.5	0.0033
62b	A → G	1211	0.00076	113.0	30.5	0.0031
65b	C → G	1059	0.00081	94.2	22.1	0.0050
66a	+ACTTCG	1240-1241	0.00080	15.9	16.0	0.037
67a	C → T	136	0.00079	0.006	11.5	0.023
68a	C → T	815	0.00076	0.087	14.3	0.090
69a	-CAA	864-866	0.00077	0.034	11.2	0.078
70a	A → C	793	0.00079	62.9	20.2	0.012
70b	-TCGCAGGGTAAAGGGCTG	796-813	0.00079	0.19	13.4	0.010
71a	A → C	793	0.00075	0.24	15.5	0.014
71b	G → T	809	0.00077	0.0045	14.7	0.0026
94a	-ACCGATCCGGCC	304-315	0.00087	42.8	11.8	4.2
95a	G → A	821	0.00075	0.27	13.8	0.0084
96a	A → T	760	0.0011	160	17.3	0.017
96b	A → C	581	0.00072	0.4	16.4	0.0054
97b	A → C	580	0.00076	0.04	12.8	0.057
98a	deletion & insertion	704-719	0.00077	0.12	14.3	0.010
99a	A → G	560	0.00074	0.04	12.9	0.0090

Supplementary Table 2 – Typical parameter estimates obtained using the data in Supplementary Figure 15 for the wild-type *E.coli* B(REL606) strain. The quoted p-value is for a one-sided t-test that the parameter is zero, or not (t-values as indicated, $n = 45$). Parameters $c_{\rm hi}$, $c_{\rm lo}$ and p were determined in the same manner as Supplementary Figure 14. Do note that $c_{\rm hi}$ is a theoretical upper bound that emerges from the data fitting process, it is not a value for yield that can be necessarily realised by *E.coli*, whereas yields above $c_{\rm lo}$ are realised in practise.

parameter	**estimate**	**standard error estimate**	**coefficient of variation**	**T value**	**p value**
$V_{\max}$ (or V) [per cell per h]	$2.8 \cdot 10^{-6}$	$3.06 \cdot 10^{-7}$	0.109	9.14	$1.59 \cdot 10^{-11}$
K_m (or K) [μg/ml]	57.2	11.8	0.207	4.83	$2.75 \cdot 10^{-5}$
$c_{\rm hi}$ [cells/μg]	$1.67 \cdot 10^8$	$7.11 \cdot 10^7$	0.426	2.35	0.0279
$c_{\rm lo}$ [cells/μg]	$6.81 \cdot 10^5$	$2.4 \cdot 10^4$	0.0352	28.4	$4.39{\cdot}10^{-30}$
p [ml/μg]	15.3	6.98	0.455	2.2	0.038

Supplementary Discussion

A: Trade-Off Theories of Adapting Consumer-Resource Dynamics

1. Concavity and convexity: bounding the number of quasi-species

We begin with a theoretical derivation of the relationship between trade-off geometry and the diversity of strategies supported by a population. To do this we used an elegant formulation based on a diffusion equation phenomenology where consumers reside on a continuum of traits and seek to exploit two extracellular resources. In this model, the one-parameter family of consumers can adopt a range of survival strategies that allow it to access the pair of resources that are required for replication. These consumer phenotypes are denoted by x and, of the two resources available, the concentration of each in the environment is denoted R_1 and R_2, respectively. We assume each consumer, with phenotype x, has density $C(t,x)$ at time t and we suppose that a consumer 'cell' encounters resources 'molecules' at a rate proportional to both the density of cells and the concentration of the available molecules. Finally, x represents the probability that R_1 is utilized by $C(x,t)$ at such an encounter.

Two important assumptions remain: first, the more able consumers of the first resource are less able to consume the second resource. This imposes a condition that if $\tau(x)$ is the probability of phenotype x consuming, and therefore metabolising, R_2 when an encounter arises between the two, then $\tau(x)$ is a decreasing function such that $\tau(0) = 1$ and $\tau(1) = 0$. Finally, we assume some consumers, irrespective of phenotype, can adapt their consumption strategy (x) at any time. This fraction is controlled by a volatility parameter denoted σ.

If we further assume that turnover ensures both consumers and resources are lost at rate d, where the resources are replenished at rate ρ, then one dynamical system representing the evolution of the population of consumers is given by following the integro-partial differential equation:

$$\frac{\partial}{\partial t}C = \sigma\frac{\partial^2}{\partial x^2}C + (xR_1 + \tau(x)R_2 - d)C, \tag{1a}$$

$$\frac{d}{dt}R_1 = \rho - R_1\int_0^1 xC(t,x)dx - dR_1, \tag{1b}$$

$$\frac{d}{dt}R_2 = \rho - R_2\int_0^1 \tau(x)C(t,x)dx - dR_2. \tag{1c}$$

This is subject to the boundary condition that no consumer is allowed to ingest resource one with probability less than zero or greater than one, meaning

$$0 = \frac{\partial C}{\partial x}(t,0) = \frac{\partial C}{\partial x}(t,1) \qquad \forall t > 0. \tag{1d}$$

Here time has been scaled so the number of encounters per unit time between resource and consumer is unity.

Supplementary Remark 1. *We begin this discussion with a two-resource model because most prior theory on species coexistence is based on the existence of multiple extracellular nutrients. However, do note that the models that we ultimately use to predict the coexistence of multiple (three) bacterial genotypes, as discussed in the main text and later in this document, are predicated only on a single resource environment (i.e. one extracellular nutrient).*

Equation (1) is not mathematically straightforward but it has been partially addressed[2] assuming, not unreasonably, that its solutions converge to steady-state. In this case a series of simplifications ensue, as follows. First, we can consider R_1 and R_2 as constant, if unknown, values depending on systemic parameters. From this we deduce

$$-\sigma\frac{1}{C}\frac{\partial^2 C}{\partial x^2} = xR_1 + \tau(x)R_2 - d. \tag{2}$$

As C is positive, describing a density, (2) informs us of where $C(x)$, the equilibrium distribution, is convex and concave, this is determined entirely by $\tau(x)$, and we can now infer how many quasi-species of consumers C can contain in equilibrium.[2] See Supplementary Figure 1 for an illustration of an evolutionary branching event in this framework obtained when $\tau(x)$ is concave.

So, suppose d is constant and suppose too that $\tau(x)$ is concave. Noting that quasi-species are values of x where $C(x)$ has a local maximum, an argument using only elementary calculus[2] shows that there can be no more than one quasi-species of (1) if $\tau(x)$ is concave. One can also show that there can be no more than two quasi-species if $\tau(x)$ is convex. This framework does not imply that concavity leads to two quasi-species, just that concavity is a necessary condition for two steady-state quasi-species to exist in steady-state. Thus, if a mathematical theory based on a diversity of consumers constrained by resource-consumption trade-offs is to support three or more quasi species

in steady-state, then the trade off, here denoted $\tau(x)$, would have to be neither concave nor convex, but instead have a 'staircase' form with different regions within which $\tau(x)$ were concave and convex.

1.1. **Optimising linear functionals over 2-d domains.** Different arguments support the theory that convex trade-offs lead to unique evolutionary optima. Consider the abstract situation whereby a two-dimensional set of traits, (x, y), is associated with a fitness value $\ell(x, y)$ where the latter depends linearly on x and y, say $\ell(x, y) = ax+by$ where $a, b > 0$ are positive parameters. We assume that the traits selected for by evolution are those that maximize the value of ℓ but those traits necessarily lie in a bounded set of biologically feasible values denoted Ω.

As ℓ is linear it can have no extrema in the interior of Ω and so the successful traits necessarily lie on the boundary of Ω which, note, is a one-dimensional curve that plays the role of a trade-off (in Supplementary Figure 2 this boundary is described locally by a function $y = T(x)$). Thus, along the set of possible optima, the fitness values are described by

$$\ell(x, y) = \ell(x, T(x)) = ax + bT(x) \tag{3}$$

and the optima therefore occur when $\frac{d}{dx}\ell(x, T(x)) = \frac{d}{dx}(ax + bT(x)) = a + bT'(x) = 0$. For this optimum to be a maximum we also require $T''(x) < 0$. If the latter inequality holds everywhere there cannot be two points at which $\ell(x, T(x))$ has a local maximum because $a + bT'(x) = 0$ must then hold at two values of x, a fact that follows from the mean value theorem of elementary calculus. It is therefore only when $T''(x)$ changes sign that there can be two optima of ℓ over Ω.

Note that the meaning of equations (2) and (3) are entirely analogous and the predictions made by a diffusion equation approach within a resource-consumption framework and an optimality approach, as regards the importance of trade-off shape, appear identical. It is worth re-iterating that both frameworks do not guarantee the simultaneous coexistence of two phenotypic traits if the trade-off is non-convex, merely that non-convexity of trade-offs is a necessary condition for coexistence.

B: Mathematical Derivations of Trade-Off Geometries

2. Not quite a rate-affinity trade-off

Having established the importance of trade-off geometry to theory, we now begin a process of seeking evidence for trade-offs whose geometry can be predicted from physical principles. We do this by re-visiting a classical model for the transport of an extracellular sugar into the periplasm of a Gram-negative bacterial cell, as illustrated in Supplementary Figure 3.

2.1. **First: finding a linear rate-affinity correlation with no trade-off.** The standard model for the passive transport of a carbon source into a bacterial cell that we use takes the form

$$S_{\text{ext}} \overset{\text{diffusion}}{\longleftrightarrow} S_{\text{ads}} \underset{k_{-1}}{\overset{k_1}{\rightleftharpoons}} TS \xrightarrow{\kappa} T + S_{\text{int}}. \tag{4}$$

Here S_{ext} is the bulk concentration of an extracellular sugar that diffuses freely apart, that is, when in close proximity to a protein transporter, due, for example, to an energetically favorable interaction between sugar and transporter. We will write S_{ads} for the concentration of 'adsorbed' sugar in a neighbourhood of the transporter that will in general be different from the bulk concentration away from the cell.

This model makes several assumptions: any molecule adsorbed to the outer-membrane transporter has a non-zero probability of being translocated into the periplasm of the cell. Such a molecule could also, however, diffuse away from the cell with non-zero probability. Assuming mass action interactions between sugar molecules and the transporter protein, we obtain the following standard mathematical model for sugar transportation, with the addition of bulk sugar that diffuses at a rate determined by D:

$$\frac{d}{dt}S = D(S_{\text{ext}} - S) + k_{-1}(TS) - k_1 T \cdot S, \tag{5a}$$

$$\frac{d}{dt}T = k_{-1}(TS) - k_1 T \cdot S + \kappa(TS), \tag{5b}$$

$$\frac{d}{dt}(TS) = -k_{-1}(TS) + k_1 T \cdot S - \kappa(TS), \tag{5c}$$

$$\frac{d}{dt}S_{\text{int}} = \kappa(TS), \tag{5d}$$

where we write $S \equiv S_{\text{ads}}$ to simplify notation. The purpose of the following calculation is to answer the question: does this model contain a trade-off?

To answer this, first note that $T(t) + (TS)(t) = T(0) + (TS)(0) =: T_0$, so the number of transporters is assumed to be constant in number throughout what follows. If we assume (5a-d) is in steady-state, by adding (a) and (c) we deduce that

$$(TS) = \frac{D(S_{\text{ext}} - S)}{\kappa} \qquad \text{and therefore} \qquad \frac{d}{dt}S_{\text{int}} = D(S_{\text{ext}} - S).$$

Thus the rate of sugar accumulation in the periplasm is proportional to the difference in concentration between the bulk sugar and the adsorbed sugar.

We now want to express S in steady-state as a function of S_{ext}. From (5c) we obtain $(TS) = \frac{k_1 T \cdot S}{k_{-1}+\kappa}$ but $T = T_0 - (TS) = T_0 - D(S_{\text{ext}} - S)/\kappa$ and so comparing the different expressions we have found so far for (TS), we find

$$(TS) = \frac{D(S_{\text{ext}} - S)}{\kappa} = \frac{k_1 T \cdot S}{k_{-1} + \kappa} = \frac{k_1 \left(T_0 - D(S_{\text{ext}} - S)/\kappa\right) \cdot S}{k_{-1} + \kappa}.$$

This looks unhelpful, so we simplify further:

$$\frac{k_{-1} + \kappa}{k_1}(S_{\text{ext}} - S) = \left(\frac{\kappa T_0}{D} - (S_{\text{ext}} - S)\right) \cdot S,$$

but the latter is a quadratic equation in S that we can write as

$$q(S) := S^2 + S(a + b - S_{\text{ext}}) - aS_{\text{ext}} = 0,$$

where $a = \frac{k_{-1}+\kappa}{k_1}$ and $b = \frac{\kappa T_0}{D}$. A positive root of $q(S)$ now defines S as a function of S_{ext}, this will be written $S(S_{\text{ext}})$.

As $q(0) = -aS_{\text{ext}} < 0$ and $q(S_{\text{ext}}) = bS_{\text{ext}} > 0$, it follows that the positive branch, $S(S_{\text{ext}})$, satisfies

$$0 < S(S_{\text{ext}}) < S_{\text{ext}}.$$

Thus the adsorbed sugar concentration can be no greater than the bulk sugar supply concentration, because the sugars are translocated when in the vicinity of the transporter. Now, solving $q(S) = 0$ explicitly we can write

$$S = S(S_{\text{ext}}) = \frac{1}{2}\left(S_{\text{ext}} - (a+b) + S_{\text{ext}}\left(\left(1 - \frac{a+b}{S_{\text{ext}}}\right)^2 + \frac{4a}{S_{\text{ext}}}\right)^{1/2}\right),$$

thus $S(S_{\text{ext}}) = S_{\text{ext}} + O(1)$ when S_{ext} large and, moreover, when $S_{\text{ext}} = 0$ it follows that $S = 0$ too, as it must.

Differentiating $q(S(S_{\text{ext}})) = 0$ with respect to S_{ext} and using a prime ($'$) to denote such a derivative, we find that

$$0 \equiv \frac{dq}{dS}S' + \frac{dq}{dS_{\text{ext}}} = 2SS' + S'(a + b - S_{\text{ext}}) + S \times (-1) - a$$

and so $S' = 0$ can only occur if $S(S_{\text{ext}}) + a = 0$. For $S, a > 0$ this is a contradiction which ensures that $S(\cdot)$ is a monotone increasing function. Moreover, setting $S_{\text{ext}} = 0$ into the above expression for the derivative of $q(\cdot)$ shows that $S'(0)(a + b) - a = 0$, or $S'(0) = a/(a + b)$. Hence

$$S(S_{\text{ext}}) = \frac{a}{a+b}S_{\text{ext}} + O(S_{\text{ext}})^2$$

for small S_{ext}.

This information completes our calculation. Using $T_0 = T + (TS) = T + T \cdot Sk_1/(k_{-1} + \kappa)$ we now obtain $T = \frac{T_0}{1+kS}$ where $k = k_1/(k_{-1} + \kappa)$ and from (5c) it follows that $(TS) = kT \cdot S$. We have thus derived an expression for the uptake rate of sugars into the periplasm as a function of the external concentration of that sugar:

$$\frac{d}{dt}S_{\text{int}} = \kappa(TS) = \kappa kT \cdot S = \frac{\kappa T_0 S}{k^{-1} + S} = \frac{\kappa T_0 S(S_{\text{ext}})}{k^{-1} + S(S_{\text{ext}})} \tag{6a}$$

$$\leq \frac{\kappa T_0 S_{\text{ext}}}{k^{-1} + S_{\text{ext}}}. \tag{6b}$$

So, the rate of transportation of sugar has the expected Michaelis-Menten form in (6a) but with an environmentally-dependent correction that accounts for the diffusion of sugar away from the cell membrane, reducing uptake to a value below its classical value, given by (6b). This is consistent with other work which shows that diffusive modifications to the classical Michaelis-Menten uptake model can lead to changes in predicted uptake rates.[3]

Importantly, this model possesses a rate-affinity correlation although, as we explain, this is not a trade-off. To see this let V be the maximal rate of uptake of sugar,

$$V := \max_{S_{\text{ext}} \geq 0} \frac{\kappa T_0 S(S_{\text{ext}})}{k^{-1} + S(S_{\text{ext}})} \overset{\text{by def.}}{=} \kappa T_0,$$

which follows from the properties of $S(S_{\text{ext}})$. The half-saturation constant, K, is then defined to be the value of S_{ext} for which half-maximal uptake is attained. This is the value of S_{ext} for which

$$\frac{1}{2}V = \frac{\kappa T_0 S(S_{\text{ext}})}{k^{-1} + S(S_{\text{ext}})}.$$

As a result, K is defined by the condition $S(K) = k^{-1}$ which occurs by definition when $q(k^{-1}) = 0$ and $S_{\text{ext}} = K$. Thus $k^{-2} + k^{-1}(a + b - K) - aK = 0$, or

$$K = \frac{1 + k(a+b)}{k^2 a + k} = \frac{2 + kb}{2k} = \frac{1}{k} + \frac{b}{2},$$

because $a = k^{-1}$. Using $k^{-1} = (k_{-1} + \kappa)/k_1 = (k_{-1} + V/T_0)/k_1$, it follows that

$$K = \frac{k_{-1} + \frac{1}{T_0}V}{k_1} + \frac{V}{2D} = \frac{k_{-1}}{k_1} + \left(\frac{1}{T_0 k_1} + \frac{1}{2D}\right)V.$$

At this point we are a little swamped by notation. So, to put this more straightforwardly, given the assumptions of this simple transportation model, we have found physiological constants α and β such that K has an affine dependence on V:

$$K(V) = \alpha + \beta V. \tag{7}$$

As then affinity, which is defined by V/K, can be negatively correlated with V depending on the value of β, (7) would seem to provide a candidate for a trade-off in terms of rate and affinity: the greater the maximal uptake rate of sugar through the transporter, the lower the affinity (and the higher the half saturation constant) of that transporter.

However, when we inspect the rate of sugar import into the periplasm,

$$\frac{d}{dt}S_{\text{int}} = \frac{V \cdot S(S_{\text{ext}})}{K(V) + S(S_{\text{ext}})}, \tag{8}$$

the affine nature of K with respect to V means this import rate is an increasing function of V for all sugar concentrations:

$$\frac{\partial}{\partial V}\left(\frac{d}{dt}S_{\text{int}}\right) = \frac{\partial}{\partial V}\frac{V \cdot S(S_{\text{ext}})}{K(V) + S(S_{\text{ext}})} = \frac{\alpha + \beta V}{(K(V) + S(S_{\text{ext}}))^2} > 0.$$

In other words, an increase in the maximal possible uptake rate of sugar by the transporter, due to a mutational or regulatory change that alters one of the physical parameters defining α and β, leads to a concomitant increase in the uptake rate of sugar at all extracellular sugar concentrations. So, despite the increase in half saturation constant K with increasing V, this is not a sufficiently severe increase to be deemed a rate-affinity trade-off because any increase in V increases sugar import rates at all sugar concentrations.

Supplementary Remark 2. *At this point we clarify a point of terminology that we adopt throughout, whereby the term 'affinity' is used for the parameter V/K. There are formulations of resource-uptake functions in which affinity, $a := V/K$, is explicitly defined and given by the derivative of that function, $U(S)$, at $S = 0$. For example, one could write the Monod-Michaelis-Menten function describing uptake as*

$$U(S) = \frac{aVS}{V + aS} = \frac{VS}{\boxed{V/a} + S},$$

where $U(\infty) = V$ and $U'(0) = a$, and so the parameter a is explicit. The half-saturation constant (usually written K) is highlighted with a box. The fact that $U'(0) = a$ illustrates why $a = V/K$ is usually seen as the affinity parameter: a controls the rate of increase in uptake rate at very low sugar concentrations.

3. A nonlinear $K(v)$ relationship: the rate-affinity trade-off (the RATO)

The point we make in the previous section that a linear $K - V$ relationship is not a rate-affinity trade-off requires further clarification. Take a Michaelis-Menten import function of the general form

$$\frac{d}{dt}S_{\text{int}} = \frac{V \cdot S}{T(V) + S},$$

where $T(V)$ is the half-saturation constant and S could be a function of S_{ext}. We are writing '$T(V)$' here to remind us that we are seeking conditions under which this function is a trade-off. Now, a rate-affinity trade-off is said to occur when an increase in the maximal import rate V produces an increase in half saturation $T(V)$ so severe that the import rates by the transporter will decrease at some sugar concentrations.

So, while increasing V will always increase $\frac{d}{dt}S_{\text{int}}$ for high enough extracellular sugar concentration because $VS/(T(V) + S)$ asymptotes towards V at large S, there could be a cost associated with this improvement given by a reduction in $\frac{d}{dt}S_{\text{int}}$ at lower extracellular sugar concentrations. *This* is the trade-off we seek. The question we have now is what biologically-relevant modification of the model defined by (5) will achieve this?

In order to obtain some information on what $K - V$ relationships can form trade-offs, imagine there are two different cell genotypes with different transporter structures that each have maximal uptakes rates V and V' where $K = T(V)$ and $K' = T(V')$, respectively, are the half-saturation constants. For a rate-affinity trade-off to occur, it is necessary that the functions defining the respective sugar import rates for both genotypes (i.e. $VS/(T(V) + S)$ and $V'S/(T(V') + S)$) have a point where they cross, as illustrated in Supplementary Figure 4(right).

So, while $V > V'$ implies $\frac{V \cdot S}{T(V)+S} > \frac{V' \cdot S}{T(V')+S}$ when S is large, this inequality must be reversed for some values of S if there is to be a rate-affinity trade-off between these two cell genotypes. Hence there must be a sugar concentration S for which $\frac{V \cdot S}{T(V)+S} = \frac{V' \cdot S}{T(V')+S}$. A little algebra shows that if this crossing point exists, it occurs when

$$S = (VT(V') - V'T(V))/(V' - V). \tag{9}$$

It is easy to see that condition (9) cannot be satisfied in the biologically relevant regime $S \geq 0$, if T has the affine form $T(V) = \alpha + \beta V$ with α and β both positive, this affine function is not able to produce a rate-affinity trade-off. A quadratic function whereby $T(V) = \alpha + \beta V + \gamma V^2$ can, however, produce such a solution but what structure in the cell might lead to such a nonlinear form? We now address this question.

3.1. **A nonlinear $K(v)$: transport across both outer and inner membranes.** The periplasm of Gram-negative bacteria is separated by two lipid bilayers that sugars must be transported through in order to gain entry to the cytoplasm of the cell where they can be metabolized. Thus, these bacteria have not one transporter for maltotriose but two that form a serial pathway. The first is the product of the gene *lamB* that brings maltotriose into the periplasm through the outer leaflet of the membrane, the protein product of *malFGK* then actively transports this sugar into the cytoplasm at an ATP cost.

The prior transport model, equation (5), must therefore be modified to account for this additional complexity. We therefore write a new uptake schema of the form:

$$\begin{array}{l} S_{\text{ext}} \overset{\text{diffuse}}{\longleftrightarrow} S_\alpha \underset{k_{-1}}{\overset{k_1}{\rightleftharpoons}} T_1S_\alpha \xrightarrow{\kappa_1} T_1 + S_{\text{per}} \\ \qquad\qquad\qquad\qquad\qquad\qquad\qquad\qquad \downarrow \\ \qquad\qquad\qquad\qquad\qquad\qquad\qquad\qquad S_{\text{per}} \overset{\text{diffuse}}{\longleftrightarrow} S_\beta \underset{k_{-2}}{\overset{k_2}{\rightleftharpoons}} T_2S_\beta \xrightarrow{\kappa_2} T_2 + S_{\text{cyt}}. \end{array} \tag{10}$$

This neglects the ATP cost of transportation as this would increase the complexity of the model substantially. Nevertheless, as we now show, (10) is sufficient to produce the nonlinear form for $K(V)$ necessary to observe the existence of a rate-affinity trade-off.

As before, sugar is held in bulk at concentration S_{ext} and it can also be adsorbed to the cell surface, at concentration S_α. The sugar is then transported into the periplasm and it can diffuse there, at mean concentration S_{per}, before adsorbing to a transporter in the inner membrane, at concentration S_β, from where it is translocated into the cytoplasm. The following mathematical model represents this cascade, with the concentration of sugars in the cytoplasm denoted by S_{cyto}:

$$\frac{d}{dt}S_\alpha = D_{\text{ext}}(S_{\text{ext}} - S_\alpha) + k_{-1}(T_1S_\alpha) - k_1T_1 \cdot S_\alpha, \tag{11a}$$

$$\frac{d}{dt}T_1 = k_{-1}(T_1S_\alpha) - k_1T_1 \cdot S_\alpha + \kappa_1(T_1S_\alpha), \tag{11b}$$

$$\frac{d}{dt}(T_1S_\alpha) = -k_{-1}(T_1S_\alpha) + k_1T_1 \cdot S_\alpha - \kappa_1(T_1S_\alpha), \tag{11c}$$

$$\frac{d}{dt}S_{\text{per}} = \kappa_1(T_1S_\alpha) - D_{\text{peri}}(S_{\text{per}} - S_\beta), \tag{11d}$$

$$\frac{d}{dt}S_\beta = D_{\text{peri}}(S_{\text{per}} - S_\beta) + k_{-2}(T_2S_\beta) - k_2T_2 \cdot S_\beta, \tag{11e}$$

$$\frac{d}{dt}T_2 = k_{-2}(T_2S_\beta) - k_2T_2 \cdot S_\beta + \kappa_2(T_2S_\beta), \tag{11f}$$

$$\frac{d}{dt}(T_2S_\beta) = -k_{-2}(T_2S_\beta) + k_2T_2 \cdot S_\beta - \kappa_2(T_2S_\beta), \tag{11g}$$

$$\frac{d}{dt}S_{\text{cyto}} = \kappa_2(T_2S_\beta), \tag{11h}$$

Here D_{peri} is the diffusion coefficient of sugar in the periplasm, T_1 and T_2 represent each transporter, and each of the kinetic or rate parameters k_* and κ_* are defined in the schema (10).

If, as before in §2.1, we define two parameters $a_2 = \frac{k_{-2}+\kappa_2}{k_2}$ and $b_2 = \frac{\kappa_2 T_{(0,2)}}{D_{\text{peri}}}$ and then set

$$q_2(S) := S^2 + S(a_2 + b_2 - S_{\text{per}}) - a_2S_{\text{per}} = 0,$$

a calculation entirely analogous to one presented in §2.1 shows that

$$\frac{d}{dt}S_{\text{cyto}} = \kappa_2(T_2S_\beta) = \frac{\kappa_2k_2}{\kappa_2 + k_{-2}}T_2 \cdot S_\beta = \frac{\kappa_2T_{(0,2)}S_\beta}{a_2 + S_\beta} = \frac{\kappa_2T_{(0,2)}S_\beta(S_{\text{per}})}{a_2 + S_\beta(S_{\text{per}})}. \tag{12}$$

Here $T_2(t) + (T_2S_\beta)(t)$ is a constant that is equal to the value $T_2(0) + (T_2S_\beta)(0) =: T_{(0,2)}$ and a solution of $q_2(S_\beta) = 0$ defines the function $S_\beta(S_{\text{per}})$.

Now (12) expresses the rate of entry of sugar into the cytoplasm as a function of that sugar in the periplasm, but we now need to express both as a function of sugar in the extracellular environment. Thus expressing S_{per} as a function of S_{ext} is our next step.

Adding (11a) and (11c), both assumed to be in steady-state, we obtain $D_{\text{ext}}(S_{\text{ext}} - S_\alpha) = \kappa_1(T_1S_\alpha)$ but from (11c)

$$(T_1S_\alpha) = \frac{k_1}{k_{-1} + \kappa_1}T_1 \cdot S_\alpha = \frac{1}{a_1} \cdot T_1 \cdot S_\alpha$$

where $a_1 := \frac{k_{-1}+\kappa_1}{k_1}$.

Now $T_1(t) + (T_1 S_\alpha)(t)$ is a constant so we define $T_{(0,1)} := T_1 + (T_1 S_\alpha) = T_1 + T_1 \cdot S_\alpha/a_1$ and therefore $T_1 = T_{(0,1)} a_1/(a_1 + S_\alpha)$. We deduce that

$$D_{\text{ext}}(S_{\text{ext}} - S_\alpha) = \kappa_1 T_{(0,1)} \cdot \frac{a_1 S_\alpha}{a_1 + S_\alpha}$$

which can be re-written as a quadratic equation

$$q_1(S_\alpha) := S_\alpha^2 + S_\alpha(a_1 + b_1 - S_{\text{ext}}) - a_1 S_{\text{ext}} = 0,$$

where $b_1 := T_{(0,1)}\kappa_1/D_{\text{ext}}$. The positive branch of $q_1(S_\alpha) = 0$ now defines S_α as a function of S_{ext}. From (11d) in equilibrium,

$$S_{\text{per}} - \overbrace{S_\beta}^{S_\beta(S_{\text{per}})} = \frac{\kappa_1}{D_{\text{peri}}}(T_1 S_\alpha) = \frac{\kappa_1}{a_1 D_{\text{peri}}} \cdot T_1 \cdot S_\alpha = \frac{\kappa_1 T_{(0,1)}}{a_1 D_{\text{peri}}} \cdot \frac{a_1 S_\alpha}{a_1 + S_\alpha}$$

which is sufficient to express S_{per} as a function of S_{ext} in principle.

To find the half saturation constant, K, of (12) and relate it to the maximal uptake rate, V, first note from (12) that

$$V := \kappa_2 T_{(0,2)} \cdot \max_{S_{\text{ext}} \geq 0} \frac{S_\beta(S_{\text{per}})}{k_2^{-1} + S_\beta(S_{\text{per}})} \leq \kappa_2 T_{(0,2)}.$$

Let us not be concerned for the moment whether or not equality is achieved here and define $v := \kappa_2 T_{(0,2)} = b_2 D_{\text{peri}}$. The half-saturation constant, K, is then the value of S_{ext} for which $S_\beta(S_{\text{ext}}) = k_2^{-1}$, and so we can write down three equations that define relationships between the system parameters at which half-saturation is achieved, namely:

$$q_1(S_\alpha)|_{S_{\text{ext}}=K} = 0,\ q_2(k_2^{-1}) = 0, \qquad S_{\text{per}} = k_2^{-1} + \frac{\kappa_1 T_{(0,1)}}{a_1 D_{\text{peri}}} \cdot \frac{a_1 S_\alpha}{a_1 + S_\alpha}.$$

The first two of these equations are quadratics and so

$$S_\alpha^2 + S_\alpha(a_1 + b_1 - K) - a_1 K = 0, \tag{13a}$$

$$(k_2^{-1})^2 + (k_2^{-1})(a_2 + b_2 - S_{\text{per}}) - a_2 S_{\text{per}} = 0, \tag{13b}$$

$$k_2^{-1} + \frac{\kappa_1 T_{(0,1)}}{a_1 D_{\text{peri}}} \cdot \frac{a_1 S_\alpha}{a_1 + S_\alpha} = S_{\text{per}}. \tag{13c}$$

From (13b) we introduce constants A and B to write

$$S_{\text{per}} = \frac{1 + k_2^{-1}(a_2 + b_2)}{a_1 k_2^{-2} + k_2^{-1}} = \frac{2 + k_2^{-1} b_2}{a_1 k_2^{-2} + k_2^{-1}} =: \mathsf{A} + v\mathsf{B}$$

but then (13c) can be written, after a modification of the constants A and B that we mark with a prime,

$$\mathsf{A}' + v\mathsf{B}' = \frac{S_\alpha}{a_1 + S_\alpha} < 1 \qquad \Longrightarrow \qquad S_\alpha = \frac{a_1(\mathsf{A}' + \mathsf{B}' v)}{1 - (\mathsf{A}' + \mathsf{B}' v)}.$$

If we assume for the moment that $\mathsf{A}' + \mathsf{B}' v \ll 1$ so that $S_\alpha \approx \mathsf{A}'' + \mathsf{B}'' v$, it follows from (13a) that we can approximate K by

$$K = \frac{S_\alpha^2 + (a_1 + b_1) S_\alpha}{a_1 + S_\alpha} \approx \frac{(\mathsf{A}'' + \mathsf{B}'' v)^2 + (a_1 + b_1)(\mathsf{A}'' + \mathsf{B}'' v)}{a_1 + \mathsf{A}'' + \mathsf{B}'' v},$$

an expression that we can re-write as $K(v) \approx \frac{\mathsf{P}v^2 + \mathsf{Q}v + \mathsf{R}}{\mathsf{S} + \mathsf{T}v}$.

Thus in the regime where v is small enough, $K(v)$ depends on v as an approximate quadratic, as v increases this approximation for K exhibits linear (strictly speaking, affine) behaviour. Finally, V and v are in proportion by a finite constant less than unity that depends on the kinetic parameters of the model, we are therefore justified in redefining the meaning of some parameters and writing $K(V) \approx \frac{\mathsf{P}V^2 + \mathsf{Q}V + \mathsf{R}}{\mathsf{S} + \mathsf{T}V}$. There are only four parameters in the model and so we may write

$$K(V) \approx \frac{\mathsf{P}V^2 + \mathsf{Q}V + \mathsf{R}}{1 + \mathsf{S}V}. \tag{14}$$

This completes our derivation of the shape of a rate-affinity trade-off (RATO) in *E.coli*.

Supplementary Remark 3. *The schema in (10) could be modified further to incorporate the role of MalE and the ATP-driven transportation process into the cytoplasm of the cell. However, as it stands, (10) represents a minimal change to the core schema given by (4) that allows for a nonlinear relationship between V and K. Moreover, adding further biological detail is very unlikely to return that relationship to the linear form (7) that is observed when the simpler schema (4) is used.*

3.2. **Transporter optimality properties.** Revisiting the rate of sugar import in (8), the nonlinear dependence of K on V means that the import rate of sugars can be a unimodal function of V, for all sugar concentrations $S > 0$. This means that, to each environment $S > 0$, we can associate a transporter and an associated uptake rate, V, that is optimal for that particular environment.

To see this, consider the logarithm of the import rate of maltotriose

$$\ln\left(\frac{d}{dt}S_{\text{int}}\right) = \ln\left(V \cdot S(S_{\text{ext}})\right) - \ln\left(K(V) + S(S_{\text{ext}})\right),$$

from where

$$\begin{aligned}\frac{\partial}{\partial V}\left(\frac{d}{dt}S_{\text{int}}\right) = 0 \quad &\iff \quad \frac{1}{V} - \frac{K'(V)}{K(V) + S(S_{\text{ext}})} = 0,\\ &\iff \quad VK'(V) = K(V) + S.\end{aligned}$$

The latter can be considered an equation for an optimal transportation rate, V, given an environmental sugar concentration S and it has a solution, $V(S)$, for each fixed $S > \inf_{V\geq 0}(VK'(V) - K(V))$, provided

$$\lim_{V\to\infty}\left(VK'(V) - K(V)\right) = +\infty. \tag{15}$$

Condition (15) fails if K is affine whereby, $K(V) = \alpha + \beta V$, but it is satisfied if $K(V) = \alpha + \beta V^p$, provided $p > 1$.

When condition (15) is satisfied by $K(V)$ and $VK'(V) - K(V)$ is strictly monotone increasing in V we deduce the promised optimality principle: for each value of the external maltotriose concentration, S_{ext}, because $\frac{d}{dt}S_{\text{int}} = (V \cdot S(S_{\text{ext}}))/(K(V) + S(S_{\text{ext}}))$, there is an optimal value of V, namely $V(S(S_{\text{ext}}))$ for which the uptake rate $\frac{d}{dt}S_{\text{int}}$ is maximized. For each environmental condition, S, to have a unique optimal maltotriose transporter configuration, so that $V(S)$ is a well-defined function, we also require $0 < (VK'(V) - K(V))' = VK''(V)$ which is the condition that $K(V)$ is convex for $V > 0$.

3.3. **Biophysical evidence of a RATO.** Related observations have been made before using empirical and theoretical models of diffusion-driven transport.[4,5] The latter reference argues that the energetically favorable attraction responsible for the high affinity of a transporter to its substrate may also serve to increase the time each molecule spends trapped, although diffusing, within a porin. As a result, other authors[4] make the same prediction we do, namely that to each small molecule (substrate) concentration, there is an optimal transporter that '*compromises between sufficiently high translocation probability and not too long blockage of the channel*'. Our analysis indicates that optimal transporter configurations are the result of a rate-affinity trade-off. Moreover, a microfluidics approach has been used to test the veracity of these predictions in the lab and [5, Figure 4(c)] shows the existence of an optimal translocation rate across a range of molecule-transporter affinities.

Optimization principles in aquatic microorganisms[6] are relevant to this discussion, so too is other data presented in the literature.[7] Both discuss the potential for a nonlinear relationship between $\mu_{\max}$, the maximal growth rate observed at a given sugar concentration, and the half-saturation constant K, see for example [6, Fig. 6]. However, even if we were to assume that uptake and growth rate, $V_{\max}$ and $\mu_{\max}$, were linearly related, their form for this trade-off would be different from ours.

Interestingly, there is a direct correspondence between [6, equation (7)] and [4, equation (6)], both of which modify the standard Michalis-Menten uptake form to include additional square-root terms that depend on physical characteristics of the transport systems under study. From [4, equation (6)] it can be deduced that translocation rate for a given concentration of external sugar, there denoted c (whereas we write this S) and assuming no internal sugar, is given by the expression

$$J_{opt}(c) = \frac{2D_bRc}{\left(1 + L\sqrt{\frac{D_bRc}{D_{ch}}}\right)^2} \implies \max_{c\geq 0} J_{opt}(c) = \frac{2D_{ch}}{L^2}$$

where the diffusion coefficient of the sugar molecule in the channel is D_{ch}, smaller than the diffusion coefficient of the molecule in bulk, D_b. This assumes a cylindrical model channel of length L and radius R. Now, c_K, the value of c for which translocation rate is equal to one half of its maximum value, is given by

$$\overbrace{c_K}^{\text{half-saturation}} = \frac{(3+2\sqrt{2})D_{ch}}{D_bRL^2} = \overbrace{\frac{(3+2\sqrt{2})}{2D_bR}}^{\text{physical constant}} \times \overbrace{\max_{c\geq 0} J_{opt}(c)}^{\text{max. uptake rate}}.$$

In other words, using our terminology, models presented in elsewhere[4,6] are consistent with a linear $K - V$ relationship.

4. The rate-yield or 'waste from haste' trade-off (the RYTO)

We now seek a basis for the rate-yield trade-off (RYTO).[8–10] Our derivation of its shape begins with the following branched pathway in which a sugar molecule or substrate, at bulk concentration S_0 within the cell, diffuses momentarily into a region where two enzymes, E_1 and E_2, are found. The substrate is then processed by the first of these enzymes to form an intermediate product, X, which may be lost due to diffusion or else further processed by E_2 into a product Y. From the first of these two steps, n molecules of 'ATP' are synthesized whereas the second step leads to the production of m molecules of ATP, the concentration of the latter denoted by A.

A schema for this can be written as follows:

$$S_0 \xleftrightarrow{D} S \underset{k_{-1}}{\overset{k_1}{\rightleftharpoons}} E_1S \xrightarrow{\kappa_1} E_1 + X + n \cdot A,$$

$$X \underset{k_{-2}}{\overset{k_2}{\rightleftharpoons}} E_2X \xrightarrow{\kappa_2} E_2 + Y + m \cdot A,$$

$$S \xrightarrow{D} \emptyset, X \xrightarrow{D} \emptyset, Y \xrightarrow{D} \emptyset.$$

This model assumes the enzymes do not diffuse, or else diffuse over a much longer timescale in relation to the smaller substrate and intermediate metabolites, given the size of these molecules this is not an unreasonable first approximation.

We now define the equilibrium yield of this pathway to be the equilibrium ATP produced per intermediate processed per unit time: this is the quantity

$$c(S_0) := \lim_{T\to\infty} \frac{1}{T} \int_0^T \frac{A(t)}{X(t)} dt.$$

Our aim is to understand the dependence of this yield on S_0 using the following mathematical model that describes the reactions in this branched pathway (see Supplementary Figure 5 for an illustration):

$$\frac{d}{dt}S = D(S_0 - S) + k_{-1}(E_1S) - k_1S \cdot E_1, \tag{16a}$$

$$\frac{d}{dt}E_1 = k_{-1}(E_1S) - k_1S \cdot E_1 + \kappa_1(E_1S), \tag{16b}$$

$$\frac{d}{dt}(E_1S) = -k_{-1}(E_1S) + k_1S \cdot E_1 - \kappa_1(E_1S), \tag{16c}$$

$$\frac{d}{dt}X = \kappa_1(E_1S) - k_2X \cdot E_2 + k_{-2}(E_2X) - DX, \tag{16d}$$

$$\frac{d}{dt}E_2 = k_{-2}(E_2X) - k_2X \cdot E_2 + \kappa_2(E_2X), \tag{16e}$$

$$\frac{d}{dt}(E_2X) = -k_{-2}(E_2X) + k_2X \cdot E_2 - \kappa_2(E_2X), \tag{16f}$$

$$\frac{d}{dt}Y = \kappa_2(E_2X) - DY, \tag{16g}$$

$$\frac{d}{dt}A = n\kappa_1(E_1S) + m\kappa_2(E_2X). \tag{16h}$$

Our logic is the following: due to the nature of sugar transportation, it is clear that higher values of S_0 in this model are the result of higher uptake rates of sugar into the cell, it therefore follows that lower ATP yield (per intermediate synthesized) results from faster uptake if we can show that $c(S_0)$ is a decreasing function of S_0. This will then be the rate-yield trade-off we seek, where rate could mean either uptake rate or growth rate of the cell.

Now, equation (16) satisfies two conservation laws, so we define two constants:

$$E_{10} := E_1(t) + (E_1S)(t) \qquad \text{and} \qquad E_{20} := E_2(t) + (E_2X)(t).$$

If we assume (16) is in equilibrium, using (16f) it follows that $(E_2X) = \frac{k_2}{k_{-2}+\kappa_2} \cdot X \cdot E_2$ and therefore

$$E_2 = E_{20}/(1 + \alpha X) \tag{17}$$

where $\alpha := \frac{k_2}{k_{-2}+\kappa_2}$. From (16d) we then deduce that $(E_1S) = (\beta E_2 + D)X/\kappa_1$ where $\beta := k_2\kappa_2/(\kappa_2 + k_{-2})$. This is sufficient to provide the second term for $\frac{d}{dt}A$ in equation (16h) as a saturating and monotone function of X because

$$m\kappa_2(E_2X) = m\kappa_2\alpha X \cdot E_2 = m\kappa_2E_{20}\frac{\alpha X}{1 + \alpha X}.$$

It follows from (16b) that $(E_1S) = \frac{k_1}{k_{-1}+\kappa_1} \cdot E_1 \cdot S$ and so we define $a := \frac{k_1}{k_{-1}+\kappa_1}$. From the above conservation laws we deduce that $E_1 = E_{10}/(1+aS)$ whence $(E_1S) = E_{10} \cdot \frac{aS}{1+aS}$. So, subtracting (16a) and (16b) we obtain $D(S_0 - S) - \kappa_1(E_1S) = 0$ which gives a relation between the bulk sugar and the concentration of sugar molecules being processed by the first step in this model metabolism: $D(S_0 - S) - \kappa_1 E_{10} \cdot \frac{aS}{1+aS} = 0$. The latter can be re-written

$$S_0 = S + \frac{E_{10}\kappa_1}{D} \cdot \frac{aS}{1+aS}$$

and, although obvious on physical grounds, it follows that $S < S_0$.

We can now express the rate of ATP production in a number of different, but equivalent ways, of which one is

$$\frac{d}{dt}A = n\kappa_1 E_{10}\frac{aS}{1+aS} \;+\; m\kappa_2 E_{20}\frac{\alpha X}{1+\alpha X}.$$

Now, contained within the calculation so far is the relationship

$$\frac{(\beta E_2 + D)X}{\kappa_1} = (E_1S) = \frac{D(S_0 - S)}{\kappa_1} = E_{10} \cdot \frac{aS}{1+aS}$$

and therefore, using (17) above that relates X and E_2,

$$X\left(\frac{\beta E_{20}}{1+\alpha X} + D\right) = \kappa_1 E_{10} \cdot \frac{aS}{1+aS} =: f(S), \tag{18}$$

where this defines $f(S)$ as a bounded, monotone function of S. Collating all the information thus far, it follows that $\frac{d}{dt}A = nX\left(\frac{\beta E_{20}}{1+\alpha X} + D\right) \;+\; m\kappa_2 E_{20}\frac{\alpha X}{1+\alpha X}$ or

$$\frac{1}{X}\frac{dA}{dt} = Dn + \frac{E_{20}}{1+\alpha X}(n\beta + m\kappa_2\alpha).$$

As we are seeking conditions which can support a trade-off, rather than enumerating all the conditions that do, for simplicity we now invoke a fast diffusion, or large D, approximation. In this regime, because $S_0 = S + f(S)/D = S + O(D^{-1})$ we can write $S \approx S_0 + O(D^{-1})$. An implicit function theorem argument applied to equation (18) for large D can now be used to show that $X = f(S_0)/D + O(D^{-2})$. As a result, the equilibrium ATP yield is the integral

$$c(S_0) = \lim_{T\to\infty}\frac{1}{T}\int_0^T \frac{A(t)}{X(t)}dt \approx Dn + D\frac{(n\beta + m\kappa_2\alpha)E_{20}}{D + \alpha f(S_0)}.$$

From the form of the function $f(S)$, we can express $c(S_0)$ in the form

$$c(S_0) = \frac{\mathsf{P} + \mathsf{Q}S_0}{\mathsf{R} + S_0} \tag{19}$$

for independent parameters P, Q and R. Since $f(S_0)$ is an increasing function of S_0, it follows that $c(S_0)$ is a decreasing function of S_0. Note that $c(S_0)$ can be re-written in the form $c(S_0) = \frac{\mathsf{P}}{\mathsf{R}+S_0} + \frac{\mathsf{Q}S_0}{\mathsf{R}+S_0}$ so that if

$$c_{\rm lo} := \lim_{S_0\to\infty} c(S_0) = \mathsf{Q} \qquad \text{and} \qquad c_{\rm hi} := c(0) = \mathsf{P}/\mathsf{R}$$

then

$$c(S_0) = c_{\rm hi} \cdot \frac{\mathsf{R}}{\mathsf{R}+S_0} + c_{\rm lo} \cdot \frac{S_0}{\mathsf{R}+S_0} = c_{\rm hi} \cdot \frac{1}{1+pS_0} + c_{\rm lo} \cdot \frac{pS_0}{1+pS_0} \tag{20}$$

where $p = 1/\mathsf{R}$. If we finally assume that the branched pathway represents a coarse-grained form of glycolysis and the TCA cycle and so its ATP yield correlates with cell yield, $c(S_0)$ is then a candidate description of the a trade-off between a cell's uptake of sugar and yield on that sugar (parameterized by the extracellular sugar concentration).

Other properties of glycolysis can enhance the strength of the RYTO. For example, the production of glucose from maltotriose by the products of maltose regulon *mal* leads to the production of acetate that can diffuse into extracellular space. But a high intracellular glucose concentration can result in excess NADH[11] that represses citrate synthase and, therefore, the TCA cycle. This regulatory property will enhance, not diminish, the RYTO, although it may also modulate its shape.

4.1. **The RYTO as a curve in the (rate, yield)-plane.** We can use the above calculation to formulate a shape of the rate-yield trade-off (RYTO), by writing growth rate, r, as the following Monod-Michaelis-Menten function of sugar supply concentration, here written S_0:

$$r(S_0) = c\frac{VS_0}{K + S_0}.$$

If we now include the dependence of c on S_0, we obtain

$$r(S_0) = \left(c_{\text{hi}} \cdot \frac{1}{1 + pS_0} + c_{\text{lo}} \cdot \frac{pS_0}{1 + pS_0}\right) \frac{VS_0}{K + S_0}.$$

This 5-parameter planar curve $(r(S_0), c(S_0))$ is the theoretical RYTO we were seeking, we now require a dataset to corroborate its shape and this is the purpose of the next section.

C: An *E.coli* B(REL606) mutant library

5. Estimating yield and growth rates of the library strains

In order to generate some of the empirical data we need to test the two trade-offs whose shape we derived above, we now turn to a bespoke library of *E.coli* B(REL606) mutants consisting of fifty-one bacterial variants, in addition to the wild-type, which possess mutations in their *lamB* gene (see Methods for experimental details on how the library was constructed). This library includes strains with a variety of mutations, including single nucleotide polymorphisms (SNPs), insertions and deletions of several nucleotide bases in *lamB*. These and other differences between the bacterial strains are detailed in Table S1. For completeness, the distribution of mutations is illustrated in Supplementary Figure 6 on a decorated wild-type trimeric LamB structure.

5.1. **Estimating metabolic parameters/phenotypes.** In order to estimate cell yields and growth rates, we require parameterized mathematical models of the growth kinetics of all the library strains, so we first need data on their growth capabilities. Therefore, each strain was cultured in planktonic conditions for one day in the absence of any competitors in order to measure the effect of the known *lamB* mutation on key growth parameters (again, see Methods). Each such culture created a 24h timeseries that we denote $b_j(t)$, with one j for each mutant, measured in units of optical density at 600nm (OD_{600nm} or just OD), where j is a label ranging from 0 to 51 where $j = 0$ denotes the wild-type data and parameter sets in what follows. Typical data is shown in Supplementary Figure 7. Mutations in this gene are known to affect the ability to uptake maltotriose, the 'sugar' or 'resource' we refer to in the remainder is therefore maltotriose, unless otherwise stated.

The parameters that are to be estimated, K_j, V_j and c_j (the half-saturation, maximal uptake and yield, respectively, of each strain genotype labelled j) can be determined approximately if we assume that $b_j(t)$ can be described by the following mathematical model:

$$\frac{d}{dt}b_j = \nu_j n_j + G_j(S)b_j,\ \frac{d}{dt}S = -U_j(S)b_j,\ \frac{d}{dt}n_j = -\nu_j n_j, \tag{21}$$

where n_j represents the density of a non-growing bacterial phenotype that switches to a vegetative state from a no-growing state at constant rate $\nu_j > 0$. This form of model is assumed because the cells are cultured in the lab after having been taken from stationary phase in overnight culture where they are in a resource-depleted environment and so may have down-regulated the maltose import system regulated by *malT*.[12]

The variable S denotes the extracellular concentration of maltotriose where $S(0) > 0$ is known from the maltotriose supplied as part of the experimental procedure. The value $b_j(0) + n_j(0)$ is the total initial population density that can also be measured in the culture device. (The value of the parameter $\lambda_j := b_j(0)/(b_j(0) + n_j(0))$ is, however, unknown and will be estimated for each growth experiment). Growth rate in this model is given by the value of $G_j(S) = c_j U_j(S)$, where c_j is the per maltotriose cell yield of the j-th genotype and the Monod-Michaelis-Menten function

$$U_j(S) := \frac{V_j S}{K_j + S} \tag{22}$$

represents the uptake rate of maltotriose into the cell in an environment where maltotriose is contained at concentration S (in $\mu g/ml$).

Physical units for the model (21) are defined as follows. It is shown in the Supplementary Methods that 1×OD unit corresponds to 3.8168×10^9 CFU per ml and $200ml$ were used for these experiments. The density units for b_j and n_j are OD which we therefore assume from Supplementary Figure 24 can be converted in a linear manner to cells per ml, time is measured in minutes, V_j is measured μg per OD per minute, c_j is measured in OD per μg and K_j in μg per ml. From here we can calculate the per minute maximal growth rate parameter, it is given by $\mu_{\max_j} := c_j \times V_j$.

The best-fit to data for the wild-type strain of the model (21) is shown in Supplementary Figure 7 where $S(0)$ takes on a range of values, from 1 to $125\mu g/ml$ (not all datasets are shown) and the analogous datafit was applied to *every* genotype for $S(0) = 10, 25$ and $250\mu g/ml$, thus producing several estimates of the phenotype (c_j, K_j, V_j, ν_j) for each strain in our library. Note that no datafit has an adjusted R^2 lower than 0.99 and a representative sample of those datafits for $S(0) = 250\mu g/ml$ is shown in Supplementary Figure 8 for all strains.

Seeking to test for the consistency of different parameters, our estimates for K_0 and V_0 (wild-type K and V phenotypes) were obtained at different sugar concentrations and Supplementary Figure 9 illustrates the consistency achieved for these parameter estimates at different maltotriose concentrations as well as the variability between replicates. The mean value (indicated ± s.e., n=42) of $K_0 = 3.57 \pm 0.64\mu g/ml$ was found by averaging across all 42

replicates at all maltotriose concentrations. The maximal value we obtained for this parameter in any one replicate was just under $11\mu g/ml$ and the lowest value estimated was $0.0006\mu g/ml$.

Supplementary Remark 4. *Note how the value of the parameter K_j in equation (22) not only controls 'smoothness' of the density data in the transition from exponential to stationary phase, but it also controls a substantial part of the exponential growth rate (this is shown in Supplementary Figure 10). Taken together with the size of the error bars in Supplementary Figure 7, these two figures indicate that differences in K of between 0 and $10\mu g/ml$ are not likely to be detectable using our modelling approach. Noting that $K_0 \approx 3.57\mu g/ml$ is the value estimated for the wild-type strain from our library, the variability in our prediction of K_0 when measured under different conditions as shown in Supplementary Figure 9 must be expected, even for one strain. However, when we consider that some strains report values in the range $10 - 150\mu g/ml$ (see Supplementary Table 1), we suspect from Supplementary Figure 10 that our approach is capable of indicating between those strains with very high and very low values of K. We return to this later using a more careful parameter estimation approach that uses a MCMC algorithm to estimate posterior distributions for these parameters.*

5.2. **Comparison parameter data with theoretical trade-off predictions: the RATO.** Using the above data and predictions of growth rate from the model (21), Supplementary Figure 11 shows predicted growth rates at all maltotriose concentrations for all of the genotypes in the library. It is noteworthy that this data shows the existence of two clusters that together resemble Supplementary Figure 4(right). This is an initial indication that the library has the potential to support trade-offs because some of the strains, like the wild-type, is estimated to have a growth rate that changes little as the maltotriose concentration changes, whereas others, like '19a' have a growth rate that varies with maltotriose supply. Consistent with this, Supplementary Figure 12 shows that the estimated (K_j, V_j) data obtained from the bacterial growth kinetics are positively correlated and consistent with the potential presence of a RATO, although shape cannot be determined from this data.

Supplementary Remark 5. *There are parametric variations that can lead to variability in parameter estimates that are associated with arbitrary choices made during the data-fitting process, particularly variation in the time, T, over which the fits in Supplementary Figure 8 are taken. To account for such variation and that the use of different values for T would not affect the presence of trade-offs in the data, we highlight Supplementary Figure 12. This shows error bars associated with the parameters K_j, V_j and $\mu_{\max_j}$ after using values $T = 400, 425, 450, 475, 500, 525$ and 550 minutes.*

The analysis of this section indicates that the *E. coli* strain library possesses a $K - V$ correlation that is positive but which is too noisy to definitively claim the existence of a RATO or to resolve its shape. For this reason, the main text contains RATO data for a series of genetically-manipulated yeast strains whose glucose import properties have been manipulated. These strains do show evidence of a RATO, including the predicted geometry. We therefore conclude that the library is consisted with the existence of a RATO, but further analysis (which includes conducting radio-labelled maltotriose uptake assays) is required to establish this definitively. In search of a further evidence of trade-offs within this library, we now turn to the RYTO.

5.3. **Comparison with theoretical trade-off predictions: the RYTO.** In order to determine the presence, or otherwise, of a rate-yield trade-off in the library we now examine population density data determined from the growth kinetics of the wild-type strain at seven different maltotriose concentrations ($S(0) \approx 1, 2, 4, 8, 16, 32, 63, 125\mu g/ml$) and we used three concentrations ($S(0) \approx 10, 25, 250\mu g/ml$) to determine the analogous dataset for all the other strains. We used this data (some of which can be found in Supplementary Figure 7 and 9) to determine cell yields per maltotriose supplied using two methods that we call the robust and naive approaches.

The naive yield estimate computes yield from the formula:

$$\text{naive yield} = \frac{1}{S(0)} \times \max_{0 \le t \le 24h} \mathsf{filter}(\mathrm{OD})(t). \tag{23}$$

In order to de-noise the experimentally measured optical density data, $\mathrm{OD}(t)$, this time-series was low-pass filtered before the maximum in (23) was determined using the `max` function in Matlab. The robust yield estimate is the value, c_j, obtained by fitting the mathematical growth model (21) to raw OD time-series.

First seeking evidence of a RYTO between strains, Supplementary Figure 13 shows the variation in yield (both robust and non-robust measures) determined for three maltotriose supply concentrations for all strains. This figure provides no evidence of such a trade off and, rather, shows a high degree of consistency of cell yield between cells. Seeking evidence of a RYTO in the bacterial library, we now turn to the more detailed growth data gathered for the wild-type *E.coli* strain.

5.4. **A within-strain RYTO: the wild-type.** We have the following initial evidence of a within-strain RYTO: Supplementary Figure 14(a) and (b) show that the functional form (20) provides a quantitatively accurate fit to wild-type yield data produced by both robust and naitve yield estimates. The same figure shows that both yield estimates are consistent at all maltoriose supply concentrations although the robust measure has lower variance between replicates, explaining our use of the term. Thus, there is evidence of a within-strain rate-yield trade-off and one that sees a loss in yield by a factor of approximately 3 as maltotriose supply ranges from $1\mu g/ml$ to $10\mu g/ml$ and beyond.

When the culture device is supplied with more than $10\mu g/ml$ of maltotriose, Supplementary Figure 14 shows no decrease in yield at the higher maltotriose concentrations tested and this observation is consistent with the absence of a between-strain rate-yield trade-off apparent in Supplementary Figure 13.

5.5. **Positive r-k correlations from wild-type growth data.** Our conclusions (on the existence of within-strain RYTO) are not dependent on the data-fitting techniques, analogous conclusions can be obtained using different analysis techniques. For example, Supplementary Figure 15 (and figures in the main text) depict the results of applying a prior analysis[13] to density data of the wild-type *E.coli* strain when cultured at different concentrations of maltotriose. This yields a range of estimates of growth rate, r, when explicitly manipulating the carrying capacity, k, and it too is consistent with the existence of a RYTO (see main text).

The datafits in Supplementary Figure 15(a) are based on the solutions of the logistic equation

$$\frac{d}{dt}x = rx(1 - x/k)$$

where x represents OD_{600nm}. The assumptions used in §4.1 are borne out by these datafits, as follows. If S_0 is maltotriose supply and we assume $k \approx c \cdot S_0$ and growth rate $r = r(S_0) = c \cdot \frac{VS_0}{K+S_0}$ then

$$\frac{k}{r} \approx c \cdot S_0 \cdot \frac{K + S_0}{cVS_0} = \frac{K}{V} + S_0 \cdot \frac{1}{V} \tag{24}$$

and so k/r should have linear (affine) dependence on S_0. Inspecting Supplementary Figure 15(b) that shows a linear regression between maltoriose concentration and the value of k/r, this figure indicates a strong correlation between k/r and S_0. The parameters V and K can be determined directly from this regression from the slope and intercept of the fitted line. The assumption of an approximately linear relationship between k and S_0 is also born out by Supplementary Figure 15(b) showing a clear, positive correlation. The main purpose of §4.1 is to understand how k/S_0 deviates subtly from linearity.

We note that the method used to produce the data given in Supplementary Table S2 is a different one from that used, for example, in Supplementary Figure 9 and the value of K reported in the former is higher for the wild-type strain than in Supplementary Table S1. In particular, the data of Supplementary Table S2 assumes a linear relationship between k/r and maltotriose in equation (24) whereas Supplementary Figure 15(b) shows that relationship appears to be nonlinear. This nonlinearity must impact on the size of the error when estimating both K and V, and the former more than the latter, as the coefficient of variation data in Supplementary Table S2 indicates.

D: Theoretical Predictions and Empirical Observations of Allele Frequency Dynamics

6. Predicting coexistence in a feast-famine environment using a RATO

6.1. **Coexistence in an uptake-only model: a 3-strain RATO.** Supplementary Figure 11 highlights five library strains that appear to be the fittest competitors in constant maltotriose environments, from the figure these are 9a, 19a, 62b, 29a and 71b. In a microcosm where maltotriose is not constant but rather but dependent on time, so that $S_{\text{ext}} = S_{\text{ext}}(t)$ is dynamic, then at each moment in time a different strain, and a different configuration of the maltoriose transporter, will be momentarily most fit. As that sugar is consumed and used for cell growth it necessarily reduces in concentration, that particular transporter will subsequently lose its favourable, most-fit status and a different transporter will soon become most fit, at least for a short while.

We predict on the basis of this verbal rationale that many different transporter structures (i.e. different bacterial strains) may be able to persist in an environment where the supply of sugar is in constant flux, sometimes high, sometimes low, and we therefore ask which of the five dominant strains identified above will be able to co-exist in one microcosm. For the remainder of the document, as we now explain, we concentrate on three: strains 9a, 19a and 62b the colours of which are used to identify each strain in the figures of this document.

To validate our expectation from Supplementary Figure 11 that these three strains form the trade-offs needed to be able to co-exist in a batch culture with a seasonal resource dynamic, we performed a series of datafits using the Matlab MCMC Toolbox to estimate the posterior distribution of the parameter values for each strain contained with the model (21). We used uninformative, uniform priors with the Metropolis-Hastings implemented as described in the `mcmcrun` m-file in the toolbox found at `http://helios.fmi.fi/~lainema/mcmc/`. A typical outcome of this procedure is shown in Supplementary Figure 16 which illustrates posterior marginal distributions of the parameters K and V for the three strains. While the maximum likelihood estimates of the (K, V) data for each strain presented in Supplementary Figure 16(a) is not significantly nonlinear, there is the possibility within the entire dataset of a (K, V) correlation consistent with the existence of a rate-affinity trade-off between these three strains.

In order to use the data in Supplementary Figure 16 to study the coexistence between the three strains in a seasonal environment we use the following mathematical model. Define the following vectors:

$$\boldsymbol{c} := (c_j), \boldsymbol{V} := (V_j), \boldsymbol{K} := (K_j), \boldsymbol{U}(S) := (U_j(S)) \text{ and } \boldsymbol{G}(S) := (G_j(S)),$$

where $G_j(S) = c_j U_j(S)$ and $U_j(S) = V_j S/(K_j + S)$ where j takes on the three values relevant to the three strains 9a, 19a and 62b. Then define a differential-difference equation, as follows. For $0 \le t \le T$ where T is the length of a season, solve

$$\frac{d}{dt}\boldsymbol{B}_i = \boldsymbol{G}(S_i)\boldsymbol{B}_i, \tag{25a}$$

$$\frac{d}{dt}S_i = -\langle \boldsymbol{U}(S_i), \boldsymbol{B}_i \rangle, \tag{25b}$$

where the boundary conditions apply for $i \ge 1$, where i denotes the index of each season

$$\boldsymbol{B}_i(0) = \eta \boldsymbol{B}_{i-1}(T),\ S_i(0) = S_0 + \eta S_{i-1}(T), \tag{25c}$$

with the initial conditions

$$\boldsymbol{B}_0(0) = \Delta \cdot (1, 1, 1)^T,\ S_0(0) = S_0. \tag{25d}$$

The boundary condition in (25c) has the following meaning: while S_0 is the sugar supplied to the microcosm anew after the end of each season, η is the fraction of sugar transferred to the next season of the microcosm that remains unspent from the previous season.

Here $S_i(t)$ is the maltotriose concentration within season i, $\boldsymbol{B}_i$ is a vector containing the densities of each bacterial genotype, S_0 is the maltotriose supply concentration (that was also written S_{ext} above) Δ is a small number representing the density of the bacterial inoculum in the first season and we assume that all genotypes are initially present in equal densities. Finally, $\eta > 0$ is a parameter representing the volume of matter that survives from one season to the next. We will use $\eta = 1\% = 0.01$ and $T = 24$ hours in the following unless otherwise stated, so that the terms 'season' and 'day' are equivalent. (Also, to ensure results are robust to experimental variation, in some of the simulations we present, η will be a uniformly distributed random variable taking values in the interval $(0, 0.05)$ with mean 0.025 and standard deviation 0.02.)

Equation (25) is completely parameterized by the data given in the right-hand column of Table 1 and we can therefore use (25) to predict which mutants in the library might coexist at different values of the maltotriose supply parameter, S_0. Representative numerical simulations of equation (25) in Figure 17(a) illustrate that the three strains

identified above can indeed persist when $S_0 \approx 300\mu g/ml$. The purpose of the next section is to test this prediction empirically.

7. Three-strain coexistence in a feast-famine environment

The results of the previous section, particularly, Supplementary Figure 17 makes a prediction we can test experimentally. We therefore co-cultured strains 9a, 19b and 62b in a laboratory microcosms containing DM media supplemented with maltotriose (see Methods for details) to understand whether these three strains would be stably co-maintained in the device.

Two comments are necessary regarding this experiment: it is impossible to conduct it *ad infinitum*, the experiment must be stopped at some point and so we can never validate stable coexistence in the manner possible when using a mathematical model; secondly, while it is present each strain will support a genetic lineage that may itself diversify into further lineages that we cannot detect using the genetic markers discussed in the appendix. However, our purpose is only to ask whether the biological mechanism underpinning the trade-offs discussed in this document are *sufficient* in themselves to support multiple co-existing lineages. This is a question we can answer using a mathematical model, although no mathematical model will ever capture the variety of adaptive changes each *E. coli* lineage will likely undergo.

7.1. **The 3-strain coexistence data.** Data obtained from co-culturing 9a, 19b and 62b at $333\mu g/ml$ of maltotriose (as described in Methods) is illustrated in Supplementary Figure 18. This shows 18-day density and frequency dynamics of the three strains, it shows that all three strains are maintained for the duration of the experiment. However, the observed dynamics are very different from those obtained using the theoretical model, as illustrated in Supplementary Figure 17. In particular, 9a dominates empirically, whereas it is the strain with the lowest equilibrium frequency in the model. A theory of strain dynamics comprising only maltotriose uptake is therefore insufficient to described the dynamics of the strains and the theory must therefore be altered.

In order to probe whether the density of each strain has reach stasis after 18 days of growth, we computed the ratio of densities for each strain on days n and $n+1$, for $n \leq 17$. This value represents the transfer-to-transfer growth rate of each strain and the resulting data is shown in Supplementary Figure 19(a). Values of unity represent stasis, or near-equilibrium behaviour, non-unity values represent an increase or a decline in strain densities. Indeed, Supplementary Figure 19(a) provides some evidence that the three strains have reach a period of stasis, giving statistics of transfer-to-transfer growth rates. None of the strain growth rates are consistently below unity in the manner that would be expected if fewer than three strains were to persist in the experimental device (whereby one strain would be lost at an exponential rate). Nor are these values above unity in the manner that would be expected were one strain to dominate in the device.

Consistent with this observation, Supplementary Figure 19(b) shows the results of applying the following serial one-way anova test to frequency data from Supplementary Figure 18. Suppose (F_j) for days $j = 0, 1, ..., N = 18$ is a time series of frequencies of one of the clones, so that each F_j is a set of replicate observations of those frequencies and here there are three replicates. Now let $\mathcal{F}_n := (F_j)_{j=N-n}^{N}$ be a backwards-in-time longitudinal sequence of sets containing empirical frequency observations for a given strain on day j. We claim significant **non** steady-state dynamics on day $N-n$ if a one-way anova can detect significant differences in the means of each such set of observations, $\mathcal{F}_n$ for $n \geq 1$, for **any** of the three strains used. Supplementary Figure 19(b) shows that this test fails and so we cannot reject the hypothesis that the dynamics are in steady-state until we reach day 10, whereupon significant changes in the mean frequencies of strain 62b can be detected with respect to later dynamics. Thus day 10 is the earliest possible day at which equilibrium frequency dynamics could be claimed, according to this test. (Nevertheless, subsequent experiments detailed below in §8.1 will show that the system cannot yet be claimed to have achieved equilibrium.)

Supplementary Figure 20 shows analogous dynamics of strain densities and frequencies in conditions when one of the strains is lost from the device, in one case exponentially rapidly (Supplementary Figure 20(b)). These experiments were conducted in different maltotriose conditions or with a different season length from those experiments illustrated in Supplementary Figure 18.

We recapitulate an important observation made above: although it predicts that the long-term coexistence of the three strains highlighted in Supplementary Figure 18 is possible, Supplementary Figure 17 does not capture the correct order of those strains in relation to the empirical data in Supplementary Figure 18. It follows that the parameterized model in equation (25) which only assumes differences in the *lamB* gene, and therefore differences in

sugar uptake, does not faithfully capture the frequency dynamics of the experimental microcosm and so that model needs to be improved.

8. Theoretical coexistence from a RATO and a RYTO

In order to find a biologically-relevant modification of equation (25) to account for the the strain frequency dynamics data in Supplementary Figure 18, we now turn to an aspect of glucose metabolism upon which our derivation of the RYTO was based. This is the derivation that lead to equation (20) that we showed to be consistent with the yield of the *E.coli* wild-type in our library in Supplementary Figure 14.

One notable difference between the dynamics of Supplementary Figure 18 in comparison with Supplementary Figure 17 is the order of the strains: in the empirical data strain 9a is dominant, present at frequencies of nearly 90% by day 18, however the same strain is present at very low frequencies in the theoretical simulations shown in Supplementary Figure 17. We must therefore find a modification of equation (25) which changes this order, but which does not assume any genetic differences in the subsequently modelled strains other than in *lamB*. This change must also have the paradoxical property that higher levels of maltotriose uptake lead to slower growth than cells with lower maltotriose uptake. However, it is exactly this property of *E.coli* metabolism that enabled a derivation of the RYTO in §4: fast uptake leads to the promotion of inefficient metabolism which reduces yield and leads to slow growth in circumstances when the carbon source is scarce.

We therefore adapt the prior mathematical model to include a form of the RYTO, as follows:

$$\frac{d}{dt}(S_{\text{ext}})_i = -\langle \boldsymbol{U}((S_{\text{ext}})_i), \boldsymbol{B}_i \rangle \,, \tag{26a}$$

$$\frac{d}{dt}\boldsymbol{S}_i = \langle \boldsymbol{U}((S_{\text{ext}})_i), \boldsymbol{B}_i \rangle - \alpha \boldsymbol{S}_i, \tag{26b}$$

$$\frac{d}{dt}\boldsymbol{A}_i = \alpha(1 - r(\boldsymbol{S}_i))\boldsymbol{S}_i - \alpha r(\boldsymbol{S}_i)\boldsymbol{A}_i \tag{26c}$$

$$\frac{d}{dt}\boldsymbol{B}_i = \alpha \cdot c \cdot r(\boldsymbol{S}_i)(\boldsymbol{S}_i + \delta_c \boldsymbol{A}_i), \tag{26d}$$

where $r(\boldsymbol{S}) = 1/(1 + \kappa \cdot \boldsymbol{S})$ and the following boundary conditions apply

$$\boldsymbol{B}_i(0) = \eta \boldsymbol{B}_{i-1}(T),\ \boldsymbol{S}_i(0) = \boldsymbol{S}_{i-1}(T),\ \boldsymbol{A}_i(0) = \boldsymbol{A}_{i-1}(T),\ (S_{\text{ext}})_i(0) = S_0 + \eta(S_{\text{ext}})_{i-1}(T) \tag{26e}$$

with the following initial conditions

$$\boldsymbol{B}_0(0) = \Delta(1,1,1)^T,\ \boldsymbol{S}_0(0) = (0,0,...,0),\ \boldsymbol{A}_0(0) = 0,\ (S_{\text{ext}})_0(0) = S_0. \tag{26f}$$

This model is phenomenological in the sense that it has not been derived from known physiological or metabolic laws, but it is based on the following assumptions that are illustrated in Supplementary Figure 21.

First, a subscript i denotes the seasons associated with each variable, beginning with $i = 0$ for the initial condition. Extracellular maltotriose, at concentration S_{ext}, is imported into cell according to Monod-Michaelis-Mented uptake that is different between the three cell strains that we are considering (and whose maximal uptake rates are defined in Table 1). Following uptake, the external sugar becomes an internal sugar that is held at a per-cell concentration in the 3-vector, $\boldsymbol{S}_i$.

Motivated by the fact that maltotriose is converted to glucose by the products of the genes regulated by *malT*, this internal sugar (that we hereafter assume to have been processed by MalT and refer to as 'glucose') is metabolized to produce 'ATP' which leads to cell growth. However, a secondary metabolite is also produced that can be thought of as an 'acetate' molecule, at concentration $\boldsymbol{A}_i$. While acetate is also further processed and also leads to the production of ATP, acetate production is inhibited by high glucose concentrations and this inhibition is determined by a function $r(\cdot)$ as stated within the model. Notice how r diverts $\boldsymbol{S}_i$ into the production of either $\boldsymbol{A}_i$ ('acetate') or $\boldsymbol{B}_i$ ('biomass') where the latter denotes the density of cells in the microcosm.

Therefore, the term $\alpha(1 - r)\boldsymbol{S}_i - \beta r \boldsymbol{A}_i$ in equation (26c) reflects the idea that $r \in (0, 1)$ is a fraction that controls how much internal glucose is converted rapidly to biomass and how much is converted into the metabolic intermediate, acetate, and the hyperbolic form of the function $r(\cdot)$ is taken from the earlier derivation of the RYTO shape in (20). The parameter α is the maximal rate at which acetate can accumulate from glycolysis, the value of δ_c is an additional biomass yield that is gained from metabolizing acetate over and above that biomass obtained from glucose alone. We further remark that equation (26) is forced to use one value of the yield parameter c for all three cells. This is done to ensure that the persistence of three different *lamB* mutants is due to, and only to, differences in cells that arise because of the *lamB* gene.

Supplementary Remark 6 (Some intuition: coexistence by virtue of being a victim of your own success)**.** *The coexistence we observe is possible because a genotype with fast maltotriose uptake can grow quickly initially when resource are plentiful but it also depletes its own environment, creating low-sugar conditions in which more efficient cells grow more quickly even though they uptake sugars more slowly. Depending on how much maltotriose is supplied, this principle can be enough for several genetic lineages to coexist, where each genetic lineage possesses a different sugar transporter structure.*

It might be possible that many genotypes can coexist by the same reasoning because the optimality principle of §3.2 makes a prediction that a seasonal environment has infinitely many potential niches, as follows. As sugars decline, at each moment in time a different transporter is momentarily most fit, thus creating a continuum of niches and the potential for many genetic lineages to be supported in a seasonal microcosm.

8.1. **Testing the theoretical predictions on coexistence frequencies.** Supplementary Figure 22 illustrates the outcome of empirically testing the equilibrium values of the strain frequencies of 9a, 19a and 62b as predicted by the mathematical model (26)(a-f) and which are stated in Supplementary Figure 21, namely $(96.1, 2.1, 1.7)\%$. For this experiment, the strains 9a, 19a and 62b were inoculated into a microcosm under identical conditions (a batch transfer protocol) as those used to produce Supplementary Figure 18, except the initial relative frequencies of the three strains were set to their predicted equilibrium values. The resulting density and frequency dynamics are shown in Supplementary Figure 22 and the null expectation, if the model predictions are correct, would be that the frequencies remain constant through time.

We tested a null hypothesis of constant strain frequencies in the data resulting from this protocol in two different ways that are illustrated in Supplementary Figure 23, as follows. Suppose (F_j) for days $j = 0, 1, ..., N = 8$ is a time series of frequencies of one of the clones, so that each F_j is a set of replicate observations of those frequencies where, again, there are three replicates. In order to determine when the frequencies are out of equilibrium we could ask for which value of $n \geq 1$ can the means of the values in $(F_j)_{j=0}^{n}$ be successfully distinguished at the $p = 5\%$ level using a one-way anova for **any** of three strains used? As a second test that is likely to be more sensitive to experimental variation, and therefore less conservative, we could also ask for what value of n can a t-test distinguish the means of F_0 and F_n?

As Supplementary Figure 23(a) shows, the first of these tests is unable to reject the null hypothesis that the frequency dynamics for all three strains are the same for a period of eight days. This is consistent with those dynamics residing at equilibrium for the entire duration of this microcosm. However, the second test *is* able to reject the same null hypothesis provided $n \geq 7$. Thus both tests are consistent with the statement that frequency dynamics remain in equilibrium for 7 days. Moreover, it is not surprising that the dynamics eventually move away from the equilibrium predicted by the mathematical model as it uses information about so few genes and *de novo* mutations are sure to render the model inapplicable eventually.

Supplementary Remark 7. *In microcosms with a seasonal feast-famine dynamic, as here, stationary phase sees the onset of a complex set of regulatory stress responses in bacteria,*[14–17] *none of which have been included in our mathematical models but which can have important evolutionary implications.*[18–20] *This is quite purposeful on our part as here we are interested in the question of whether genetic differences in a transporter might be sufficient to explain the existence of a stable polymorphism and the co-maintenance of three genetic lineages. There are many mechanisms in other genes that might also lead to the stable maintenance of polymorphisms and we contend that such differences only serve to increase, rather than diminish, the genetic diversity observed here.*

Supplementary Methods

9. Colony-forming units (CFUs) to optical density (OD_{600}) conversion

Throughout the document we refer to two different measures of bacterial density as measured in laboratory devices. In some instances we use CFUs as density units, the number of colony-forming units per millilitre, whereas plate readers used routinely in microbiology laboratories measure optimal densities, here at a wavelength of 600nm. To ensure both represent the same cell density, we present Figure 24 which shows a strong, linear correlation for both measures across a one order of magnitude density range.

From Supplementary Figure 24 we deduce that a value of 0.26OD as measured in a micro plate reader where the liquid volume is $200\mu L$, the value we use throughout, corresponds to approximately 10^9CFU per ml and this corresponds to 2×10^8 live bacterial cells. Thus 0.13 OD corresponds to 10^8 cells in our protocols and so 1 OD unit $\approx 7.6 \times 10^8$ cells which is 3.8×10^9 CFU per ml.

Supplementary References

References specific to the Supplementary Information

[1] Charbit, A. *et al.* In vivo and in vitro studies of transmembrane beta-strand deletion, insertion or substitution mutants of the escherichia coli k-12 maltoporin. *Molecular Microbiology* **35**, 777–790 (2000). URL http://dx.doi.org/10.1046/j.1365-2958.2000.01748.x.

[2] Gudelj, I., Coman, C. D. & Beardmore, R. E. Classifying the role of trade-offs in the evolutionary diversity of pathogens. *Proc. R. Soc. A* **426**, 97–116 (2006).

[3] Bonachela, J. A., Raghib, M. & Levin, S. A. Dynamic model of flexible phytoplankton nutrient uptake. *Proceedings of the National Academy of Sciences* **108**, 20633–20638 (2011). URL http://www.pnas.org/content/108/51/20633.abstract. http://www.pnas.org/content/108/51/20633.full.pdf+html.

[4] Berezhkovskii, A. M. & Bezrukov, S. M. Optimizing transport of metabolites through large channels: Molecular sieves with and without binding. *Biophysical journal* **88**, L17–L19 (2005). URL http://linkinghub.elsevier.com/retrieve/pii/S0006349505732161.

[5] Pagliara, S., Schwall, C. & Keyser, U. F. Optimizing diffusive transport through a synthetic membrane channel. *Adv Mater* **25**, 844–849 (2013).

[6] Smith, S. L., Pahlow, M., Merico, A. & Wirtz, K. W. Optimality-based modeling of planktonic organisms. *Limnology and Oceanography* **56**, 2080–2094 (2011).

[7] Wirtz, K. W. A generic model for changes in microbial kinetic coefficients. *J. Biotechnol.* **97**, 147–162 (2002).

[8] Gudelj, I. *et al.* An integrative approach to understanding microbial diversity: from intracellular mechanisms to community structure. *Ecol Lett* **13**, 1073–1084 (2010).

[9] Novak, M., Pfeiffer, T., Lenski, R. E., Sauer, U. & Bonhoeffer, S. Experimental tests for an evolutionary trade-off between growth rate and yield in E. coli. *Am Nat* **168**, 242–251 (2006).

[10] Pfeiffer, T., Schuster, S. & Bonhoeffer, S. Cooperation and competition in the evolution of ATP-producing pathways. *Science* **292**, 504–507 (2001).

[11] Walsh, K. & Koshland, D. E. J. Characterization of rate-controlling steps in vivo by use of an adjustable expression vector. *Proc Natl Acad Sci U S A* **82**, 3577–3581 (1985).

[12] Boos, W. & Shuman, H. Maltose/maltodextrin system of *Escherichia coli*: transport, metabolism, and regulation. *Microbiol Mol Biol Rev* **62**, 204–29 (1998).

[13] Fitzsimmons, J., Schoustra, S., Kerr, J. & Kassen, R. Population consequences of mutational events: effects of antibiotic resistance on the r/k trade-off. *Evolutionary Ecology* **24**, 227–236 (2010). URL http://dx.doi.org/10.1007/s10682-009-9302-8.

[14] Navarro Llorens, J. M., Tormo, A. & Martinez-Garcia, E. Stationary phase in gram-negative bacteria. *FEMS Microbiol Rev* **34**, 476–495 (2010).

[15] Finkel, S. E. Long-term survival during stationary phase: evolution and the gasp phenotype. *Nat Rev Microbiol* **4**, 113–120 (2006).

[16] Battesti, A., Majdalani, N. & Gottesman, S. The rpos-mediated general stress response in escherichia coli. *Annu Rev Microbiol* **65**, 189–213 (2011).

[17] Ihssen, J. & Egli, T. Specific growth rate and not cell density controls the general stress response in Escherichia coli. *Microbiology* **150**, 1637–1648 (2004). URL http://mic.sgmjournals.org/cgi/content/abstract/150/6/1637. http://mic.sgmjournals.org/cgi/reprint/150/6/1637.pdf.

[18] Ferenci, T. Maintaining a healthy spanc balance through regulatory and mutational adaptation. *Mol Microbiol* **57**, 1–8 (2005).

[19] Rozen, D. E., Philippe, N., Arjan de Visser, J., Lenski, R. E. & Schneider, D. Death and cannibalism in a seasonal environment facilitate bacterial coexistence. *Ecol Lett* **12**, 34–44 (2009).

[20] Kinnersley, M. A., Holben, W. E. & Rosenzweig, F. *E Unibus Plurum*: Genomic analysis of an experimentally evolved polymorphism in *escherichia coli*. *PLoS Genet* **5**, e1000713 (2009). URL http://dx.doi.org/10.1371%2Fjournal.pgen.1000713.